SimCenter

NATIONAL CENTER for COMPUTATIONAL ENGINEERING

Petrov-Galerkin and Discontinuous-Galerkin Methods for Time-Domain and Frequency-Domain Electromagnetic Simulations

A Technical Report by

W. Kyle Anderson, Li Wang, Sagar Kapadia, Craig Tanis, and Bruce Hilbert

Petrov-Galerkin and Discontinuous-Galerkin Methods for Time-Domain and Frequency-Domain Electromagnetic Simulations

W. Kyle Anderson, Li Wang, Sagar Kapadia, Craig Tanis, Bruce Hilbert

SimCenter: National Center for Computational Engineering
701 East M.L. King Boulevard, Chattanooga, TN 37403

Abstract

Finite-element discretizations for Maxwell's first-order curl equations in both the time domain and frequency domain are developed. Petrov-Galerkin and discontinuous-Galerkin formulations are compared using higher-order basis functions. Verification cases are run to examine the accuracy of the algorithms on problems with exact solutions. Comparisons with other, well accepted, methodologies are also considered for problems for which exact solutions do not exist. Effects of several parameters, including spatial and temporal refinement, are also examined and the relative efficiency of each scheme is discussed. By considering test cases previously considered by other researchers, it is also demonstrated that the algorithms developed during the current program do not exhibit spurious solutions. Finally, three-dimensional results are compared with test results for a rectangular waveguide for which experimental data has been obtained with the explicit purpose of code-validation. The ability to predict changes in scattering parameters caused by variations in geometric and material properties are examined and it is demonstrated that the algorithms predict these changes with good accuracy.

Introduction

For more than 40 years, researchers have been developing computational methods for obtaining simulation-based solutions to Maxwell's equations. One of the most ubiquitous methods for engineering applications is the Finite-Difference Time-Domain (FDTD) method first introduced by Yee in 1966 [1]. In this method, the field is discretized into a series of uniform hexahedral volumes on which the electric field intensities are stored at the centers of the square faces forming the boundaries of the cube, while the magnetic flux intensities are stored along the edges at the intersection of the faces. The spatial derivatives in the first-order form of Maxwell's equations are approximated with second-order central differences and the leapfrog method is used for temporal discretization [2]. As discussed in Ref. [2], the resulting scheme is able to maintain tangential continuity of field intensities across dissimilar materials, yields divergence-free fields for charge-free domains, and obtains non-decaying solutions for propagating waves. The simplicity of this approach has contributed greatly to its wide use in the engineering community where it has been used for analysis of many electromagnetic devices. Despite the successful application of this methodology, it suffers from several shortcomings, most notably the stability-imposed time-step limitations and the lack of fidelity in modeling non-planar surfaces or devices with a widely varying range of geometric scales.

To eliminate the "staircase" geometries typically used in the FDTD approach, finite-element methodologies have been developed for both frequency-domain and time-domain applications. The most prevalent formulations of this approach solve for either the electric or magnetic fields, with the other field variables being obtained by numerical differentiation [3]. Significant effort has gone into the development of numerical simulations based on this technique that are both accurate and efficient [3]. Furthermore, through the development of so-called "edge elements," spurious solutions that often vitiated the results obtained with earlier implementations can be avoided. While this method can be used to accurately model complex geometries, it has the disadvantage that because either the electric or magnetic field is first obtained, with the other field variables being determined in a post-processing step, the order of truncation error of the secondary field variables is one order less than that of the primary variables.

Another approach that has been used for the numerical simulation of Maxwell's equations is the finite-volume method. Here, the first-order curl form of the equations is recast into divergence form and integrated over non-overlapping control volumes where the volume integrals involving spatial derivatives are first converted to surface integrals that are subsequently evaluated numerically. In this form the matrices obtained by linearizing the flux vectors with respect to the dependent variables have real eigenvalues and a complete set of eigenvectors [4].

1

Consequently, because of the mathematical similarities between this form of Maxwell's equations and the compressible Euler equations from fluid mechanics, many of the techniques developed for fluid-dynamic problems can be applied to the solution of Maxwell's equations. In Refs. [4-9], finite-volume methods have been described taking advantage of these relationships. In recent years, this approach has been further developed and applied to difficult electromagnetic problems with complex geometries. However, in this approach the discretization of the spatial derivatives results in a scheme with only second-order accuracy, which may be insufficient for applications involving high-frequencies, particularly for electrically large structures. While the order-of-accuracy of these methods can be raised using an extended stencil [10, 11], this adds significant complexity in book keeping, and the resulting code is cumbersome to linearize when developing implicit schemes or obtaining sensitivity derivatives.

The objective of the present study is to develop solution methodologies for time-domain and frequency-domain applications that can be used in the analysis and design of large electromagnetic structures. To this end, Petrov-Galerkin (PG) and discontinuous-Galerkin (DG) methods are developed that are extendable to high-order spatial and temporal discretization, and can accurately represent complex geometries. For time-accurate simulations, fully implicit methods are used such that time-step sizes are determined by accuracy considerations and not by stability considerations. While this requires solving a sparse matrix at each time step, this approach increases robustness that is needed in an eventual design environment and is also important when combined with adaptive meshing because of potentially very large disparities in cell resolution throughout the domain.

The discontinuous-Galerkin method, originally developed for modeling neutron transport [12], has been widely used in fluid dynamics applications [13-18] and has recently been extended by numerous researchers for electromagnetic applications [16, 19-29]. The DG scheme has the advantage that it is easily implemented using higher-order temporal and spatial accuracy and the solution can be advanced using explicit time-stepping. The later advantage stems from the assumption of discontinuous field variables across element boundaries that results in mass matrices defined over individual elements instead of being globally coupled. Despite the advantages of the DG approach, in the typical implementation the field variables are stored separately for each element thereby leading to duplication of storage at the vertices of the mesh. The result is that there are more degrees of freedom when compared to methods with single-valued variables defined at the nodes. While the additional degrees of freedom clearly translate into increased computational effort on a given mesh, it is unclear whether the extra work also provides improved accuracy.

An alternative approach, also with origins in fluid mechanics, is the Petrov-Galerkin approach [18, 30-36]. Here, the field variables are stored at the vertices of the mesh and are single-valued, thereby reducing the number of unknowns when compared to the DG approach. Despite the success of this method for fluid dynamic problems, this methodology has not been widely used for electromagnetic applications, although it has been applied to second-order equations for scalar and vector potentials [37-39] and for the second-order wave equation [40].

In the present work, Petrov-Galerkin and discontinuous-Galerkin methods are developed for both time-domain and frequency-domain applications. High-order (greater than linear) spatial discretizations are used, as is fully implicit time-stepping. The effects of several discretization-related parameters are examined and the resulting schemes are evaluated against known solutions, as well as with experimental data.

Governing Equations

The physical laws describing time-dependent electromagnetic phenomena are given by Maxwell's equations

$$\nabla \times \boldsymbol{E} = -\frac{\partial \boldsymbol{B}}{\partial t} \tag{1}$$

$$\nabla \times \boldsymbol{H} = \frac{\partial \boldsymbol{D}}{\partial t} + \boldsymbol{J} \tag{2}$$

$$\nabla \cdot \boldsymbol{B} = 0 \tag{3}$$

$$\nabla \cdot \boldsymbol{D} = \rho_c \tag{4}$$

where $\boldsymbol{E}$ is the electric field intensity, $\boldsymbol{H}$ is the magnetic field intensity, $\boldsymbol{D}$ is the electric flux density, and $\boldsymbol{B}$ is the magnetic flux density. The electric current density, $\boldsymbol{J}$, and the electric charge density, ρ_c, are both zero for the applications considered here and will not be repeated. The flux densities and field intensities are related using linear constitutive relations

$$D = \varepsilon E \tag{5}$$

$$B = \mu H \tag{6}$$

where ε is the permittivity and μ is the permeability. Note also that in the present work Eqs. 3 and 4 are not considered as they will be satisfied, at least to discretization error, with the solution of Faraday's law (Eq. 1) and Ampere's law (Eq. 2) [41, 42].

For implementation, the governing equations are rewritten in a divergence form as opposed to their more commonly used curl form given by Eqs. 1-4.

$$\frac{\partial \boldsymbol{Q}}{\partial t} + \nabla \cdot \boldsymbol{F}\big(\boldsymbol{Q}\big) = 0 \tag{7}$$

$$\boldsymbol{Q} = \left(D_x, D_y, D_z, B_x, B_y, B_z \right)^T \tag{8}$$

$$\boldsymbol{F} = \hat{i}\boldsymbol{f} + \hat{j}\boldsymbol{g} + \hat{k}\boldsymbol{h} \tag{9}$$

$$\boldsymbol{f} = \left(0, H_z, -H_y, 0, -E_z, E_y \right)^T \tag{10}$$

$$\boldsymbol{g} = \left(-H_z, 0, H_x, E_z, 0, -E_x \right)^T \tag{11}$$

$$\boldsymbol{h} = \left(H_y, -H_x, 0, -E_y, E_x, 0 \right)^T \tag{12}$$

Note that with the equations written in this form, the matrices $\begin{bmatrix} A \end{bmatrix}$, $\begin{bmatrix} B \end{bmatrix}$, and $\begin{bmatrix} C \end{bmatrix}$ associated with the linearization of the flux vectors, $\boldsymbol{f}$, $\boldsymbol{g}$, and $\boldsymbol{h}$, each have real eigenvalues and a distinct set of eigenvectors [4].

For time-periodic data, Eq. 7 can be expressed in a frequency-domain formulation as

$$i\omega\tilde{\boldsymbol{Q}} + \nabla \cdot \tilde{\boldsymbol{F}}\big(\tilde{\boldsymbol{Q}}\big) = 0 \tag{13}$$

where $\tilde{Q}$ and $\tilde{F}$ are generally complex-valued variables and result from assuming time-periodic solutions.

Numerical Solution

As discussed in the introduction, it is desirable for the methodology developed during this study to accurately represent complex geometries and be amenable to high-order spatial discretization. The ability to include multiple materials throughout the domain without the occurrence of spurious solutions is also required, as is the ability to implement the resulting formulations using implicit schemes on parallel architectures. Because both time-domain and frequency-domain technologies are developed, similar discretizations are utilized to promote code reuse. To achieve these goals, Petrov-Galerkin and discontinuous-Galerkin formulations are pursued.

Both the Petrov-Galerkin and discontinuous-Galerkin methods are formulated as weighted residual methods, which can be cast in the form shown below

$$\oiiint_{\Omega} [\phi]\left(\frac{\partial \boldsymbol{Q}}{\partial t} + \nabla \cdot \boldsymbol{F} \right)\partial\Omega = 0 \tag{14}$$

where ϕ is a weighting function.

For both schemes, the domain of interest is discretized into a series of non-overlapping elements, such as triangles for two-dimensional applications and tetrahedra for three-dimensional applications. The primary differences between the Petrov-Galerkin and discontinuous-Galerkin schemes are the location of the unknowns within an element, the form of the test function, and the assumptions regarding continuity of the solution variables between the elements.

Petrov-Galerkin

In the Petrov-Galerkin finite-element approach, field variables are assumed continuous across element boundaries. Therefore, single-valued data is stored at the vertices of the elements and the solution is assumed to vary within each element according to a linear combination of polynomial basis functions

$$\boldsymbol{Q}_h = \sum_{i=1}^{n} N_i \boldsymbol{Q}_i \qquad (15)$$

Here, $\boldsymbol{Q}_h$ represents the dependent variables approximated within each element, $\boldsymbol{Q}_i$ is the corresponding data at each node of the element, and each N_i represents a basis function. The weighting function, ϕ, consists of two parts, the first part being composed of a linear combination of the same basis functions used in Eq. 15 for defining the variables within the element. The second contribution to the weighting function is a stabilizing term that provides dissipation along preferential directions to eliminate odd-even point decoupling that often occurs with the standard Galerkin scheme that is obtained if the second contribution is neglected. In the present work, the Streamlined Upwind Petrov-Galerkin (SUPG) method is used in defining the weighting function [34]

$$[\phi] = N[I] + \left(\frac{\partial N}{\partial x}[A] + \frac{\partial N}{\partial y}[B] + \frac{\partial N}{\partial z}[C] \right)[\tau] = N[I] + [P] \qquad (16)$$

$$N = \sum_{i=1}^{n} N_i c_i \qquad (17)$$

where c_i are arbitrary constants and $[\tau]$ can be obtained using the following definitions [33]

$$[\tau]^{-1} = \sum_{k=1}^{n} \left| \frac{\partial N_k}{\partial x}[A] + \frac{\partial N_k}{\partial y}[B] + \frac{\partial N_k}{\partial z}[C] \right| \qquad (18)$$

$$\left| \frac{\partial N_k}{\partial x}[A] + \frac{\partial N_k}{\partial y}[B] + \frac{\partial N_k}{\partial z}[C] \right| = [T][|\Lambda|][T]^{-1} \qquad (19)$$

Here, $[T]$ and $[\Lambda]$ are the right eigenvectors and eigenvalues, respectively, of the matrix on the left side of Eq. 19 whereas the inverse of $[T]$ is given by $[T]^{-1}$. The resulting weak statement may be written as

$$\iiint_{\Omega} \left(N \left\{ \frac{\partial \boldsymbol{Q}}{\partial t} \right\} - \boldsymbol{F} \cdot \nabla N \right) \partial\Omega + \iiint_{\Omega} [P] \left\{ \frac{\partial \boldsymbol{Q}}{\partial t} + \nabla \cdot \boldsymbol{F} \right\} \partial\Omega + \iint_{\Gamma} N \boldsymbol{F} \cdot \hat{n} \partial\Gamma = 0 \qquad (20)$$

In evaluating the volume and surface integrals, Gaussian quadrature rules are used where for polynomial representations of the dependent variables of order p, the volume integrals are evaluated using quadrature formulas appropriate for integrating polynomials of order 2p whereas surface integrals are integrated using formulas for integrating polynomials of order 2p+1 [43]. Note that because the field variables are assumed to vary continuously in the interior of the domain, the surface integral typically vanishes on the boundaries of the interior elements and need only be evaluated on the boundaries of the domain where appropriate boundary conditions are weakly enforced by incorporating them into the surface integral.

When multiple materials of differing permittivity or permeability are present in the domain, the surface integral must be evaluated at the interface between the materials because of the discontinuous jump in the tangential components of flux densities across the interface[44, 45]. To accurately capture these jumps, duplicate nodes are created on either side of the interface and the flux-difference-splitting methodology is borrowed from fluid dynamic applications for determining the normal flux on the interface [20, 22, 46]. Here, the flux on the boundary between materials is determined using a Riemann solver and given as

$$\boldsymbol{F}\left(\boldsymbol{q}_L, \boldsymbol{q}_R\right) \cdot \hat{n} = \frac{1}{2}\left[\boldsymbol{F}(\boldsymbol{q}_L) + \boldsymbol{F}(\boldsymbol{q}_R) - \left[\tilde{T}\right]\left|\tilde{\Lambda}\right|\left[\tilde{T}\right]\left[\tilde{M}\right]\Delta\boldsymbol{q}\right] \tag{21}$$

where the tilde over the matrices indicates that they are formed from average values and

$$\Delta\boldsymbol{q} = \boldsymbol{q}_R - \boldsymbol{q}_L \tag{22}$$

represents the difference in values across the interface and

$$\boldsymbol{q} = \left(E_x, E_y, E_z, H_x, H_y, H_z\right)^T \tag{23}$$

$$\left[M\right] = \left[\frac{\partial\boldsymbol{Q}}{\partial\boldsymbol{q}}\right] \tag{24}$$

Note that while flux densities, $\boldsymbol{Q}$, serve as the fundamental variables and are obtained at each mesh point during the simulations, the field intensities are used in defining the flux in Eq. 21. The motivation for this is that using jumps in the field intensities makes it possible to satisfy the jump conditions exactly whereas a similar expression using the flux densities directly can not be obtained.

Discontinuous Galerkin

For the discontinuous-Galerkin (DG) approach, there are two primary differences in the underlying assumptions when compared to the Petrov-Galerkin scheme. First, the weighting function for DG does not include the stabilization term and corresponds to that used in a standard Galerkin method.

$$\left[\phi\right] = N\left[I\right] \tag{25}$$

Second, because the standard Galerkin approach is not able to effectively damp odd-even oscillations, the solution inside each element is assumed to vary independently from the neighboring element. This allows a discontinuity to exist across the element boundaries so that the surface integral in Eq. 20 needs to be evaluated at the interface between each element in the mesh. The evaluation of this integral is performed using the same flux-difference-splitting approach described above in Eqs. 21-24. It should be noted that in the DG approach, there is no need to create additional nodes along the interface between elements with disparate material properties. Also, by treating each element in the mesh as if it has different material properties from its neighboring elements, the PG and DG algorithms are easily unified into one code by simply not adding the second term to the weight function for DG.

Note that on a given mesh, the DG approach will typically have more degrees of freedom than the PG approach. For example, in the PG approach for linear tetrahedra in three dimensions, the number of degrees of freedom corresponds to the number of vertices in the mesh. In the DG method, because the variables in each tetrahedron are stored independently from those in the neighboring tetrahedra, there will be four degrees of freedom for each element. Noting that because there are approximately six times as many tetrahedra compared to the number of vertices (nodes) in a mesh, the number of unknowns for the DG scheme will be roughly 24 times that of the PG scheme. Table 1 summarizes the relationship between the number of unknowns in a simulation for PG and DG schemes assuming linear, quadratic, and cubic elements.

5

Table 1. Approximate Degrees of Freedom for 3D Simulations on Tetrahedra		
	Petrov Galerkin	Discontinuous Galerkin
Linear	V	$4C \approx 24V$
Quadratic	$V + E \approx 8V$	$10C \approx 60V$
Cubic	$V + 2E + F \approx 17V$	$20C \approx 120V$

In the table, V represents the number of vertices in the mesh, whereas C, E, and F represent the number of tetrahedra, edges, and faces respectively. Using data derived from typical meshes, the table above reflects that there are approximately six times as many tetrahedra as there are vertices, whereas there are about seven times as many edges and twice as many faces. A similar accounting is provided in Table 2 for two-dimensional triangles where it is noted that the number of cells (triangles) and edges each account for approximately twice as many vertices in the mesh.

Table 2. Approximate Degrees of Freedom for 2D Simulations on Triangles		
	Petrov Galerkin	Discontinuous Galerkin
Linear	V	$3C \approx 6V$
Quadratic	$V + E \approx 3V$	$6C \approx 12V$
Cubic	$V + 2E + C \approx 6V$	$10C \approx 20V$

Temporal Differencing and Solution Methodology

For the PG and DG schemes in the time-domain, second-order backward differences are currently used and an approximate solution to a sparse linear system has to be solved at each time step. For this purpose, the Generalized Minimal Residual (GMRES) method [47] is used in conjunction with an incomplete LU decomposition as a preconditioner [48]. For the frequency-domain formulation the same methodology is used, although minor modifications, invoked at compiler time, have been included to account for matrices with complex entries. In the time domain, zero fill level is typically used and the residual of the linear system is reduced eight-orders of magnitude, which typically requires a Krylov subspace with 100 vectors. For the frequency domain, one level of fill is typically used along with 5-10 restarts.

Boundary Conditions

The boundary conditions are weakly enforced by incorporating them into the boundary integral in Eq. 20. On perfect conducting boundaries, the flux normal to the surface, which in the interior is given as

$$\boldsymbol{F} \cdot \hat{n} = \left\{ \begin{array}{c} -n_y H_z + n_z H_y \\ n_x H_z - n_z H_x \\ -n_x H_y + n_y H_x \\ n_y E_z - n_z E_y \\ -n_x E_z + n_z E_x \\ n_x E_y + n_y E_x \end{array} \right\} \tag{26}$$

is re-expressed to reflect the fact that the components of the electric field tangential to the boundary are zero, thereby resulting in the following flux at the surface

$$\boldsymbol{F} \cdot \hat{n} = \left\{ \begin{array}{c} -n_y H_z + n_z H_y \\ n_x H_z - n_z H_x \\ -n_x H_y + n_y H_x \\ 0 \\ 0 \\ 0 \end{array} \right\} \tag{27}$$

For port boundaries the flux is determined using the Riemann solver given by equation 21, where the data on the exterior side of the interface is obtained using a "driving" wave, and the data on the interior of the interface is obtained from the field variables. As an example, consider the 2-port iris bandpass filter shown in Fig. 1. In the center section of the figure is the actual filter, whereas a perfectly-matched layer (PML) [49-53] is placed on both the left and right sides to absorb outward moving waves. In the left PML only scattered variables are considered, while in the right PML the solution to the full wave is obtained. On the interface between the left PML and the filter, a TE_{10} wave is used to supply the energy for the simulation. For the Petrov-Galerkin scheme, duplicate nodes are required along the interface between the left PML region and the filter, similar to the technique used in treating the interface between multiple materials. To evaluate the surface integral on this interface, a separate flux is evaluated for the nodes on the left and right sides. Assuming an outward-pointing normal oriented with respect to the filter (pointing from the filter into the left PML), the functional dependence of the flux on the interface when evaluating the residual for the nodes in the PML region is given as

$$\boldsymbol{F}(\tilde{\boldsymbol{q}}_L, \tilde{\boldsymbol{q}}_R) \cdot \hat{n} = \boldsymbol{F}(\boldsymbol{q}_L - \boldsymbol{q}_D, \tilde{\boldsymbol{q}}_R) \cdot \hat{n} \tag{28}$$

whereas the residual for nodes in the filter region is computed using a flux obtained using the full-wave variables

$$\boldsymbol{F}(\boldsymbol{q}_L, \boldsymbol{q}_R) \cdot \hat{n} = \boldsymbol{F}(\boldsymbol{q}_L, \tilde{\boldsymbol{q}}_R + \boldsymbol{q}_D) \cdot \hat{n} \tag{29}$$

In these equations, a tilde over the dependent variable represents a scattered field variable so that in Eq. 28, which is used when computing the residual for the PML region, the data on the side of the interface corresponding to the filter is computed by subtracting the driving field, thereby forming a perturbation that is consistent with the scattered-field formulation within the PML. Similarly, for evaluating the surface integral in Eq. 29, the total field data is obtained in the PML region by adding the driving field to the perturbation field stored on that side of the interface. Details of the driving state variables are given below for each application.

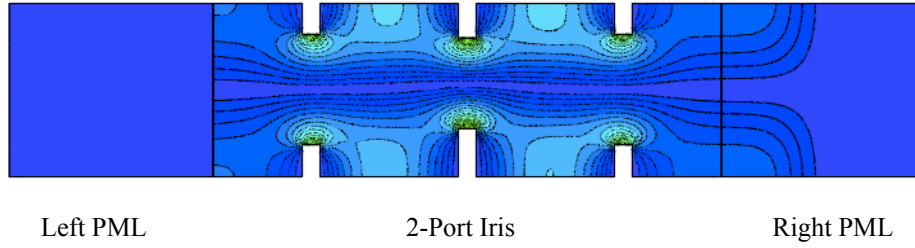Left PML   2-Port Iris   Right PML

Figure 1. Application of Boundary Conditions for Excitation of 2-Port Iris Bandpass Filter

When required, the perfectly-matched layer (PML) approach described in Ref. [53] is used for time-domain simulations, whereas that of Ref. [52] is used for the frequency domain.

Verification

Several studies have been conducted to verify that the PG and DG methods provide expected results for known datum-type solutions. In the first case, time-domain and frequency-domain solutions are obtained using the PG and DG methods and compared to an exact solution for a TM_z incident wave, with angular frequency of π, passing over a cylinder with permittivity and permeability of 2.25 and 2.0, respectively [41, 54]. The radius of the cylinder is 0.6 with the coordinates of the outer boundary extending from -1.0 to 1.0 in both directions. In Fig. 2, qualitative comparisons of the exact solution for the x-component of magnetic flux density at several times during a cycle are shown along with the corresponding contours obtained from a time-domain solution obtained using the PG method. In the figure, the top row depicts the exact solution evaluated at each node in the mesh, whereas the lower row shows contours of the numerical solution. While the figure shows results for quadratic elements, solutions with linear elements look very similar. As seen in the figure by comparing details of the contours, excellent qualitative agreement is obtained between the simulations and the exact solution.

| Exact Solution $t = 0$ | Exact Solution $t = \pi/2$ | Exact Solution $t = \pi$ | Exact Solution $t = 3\pi/2$ |

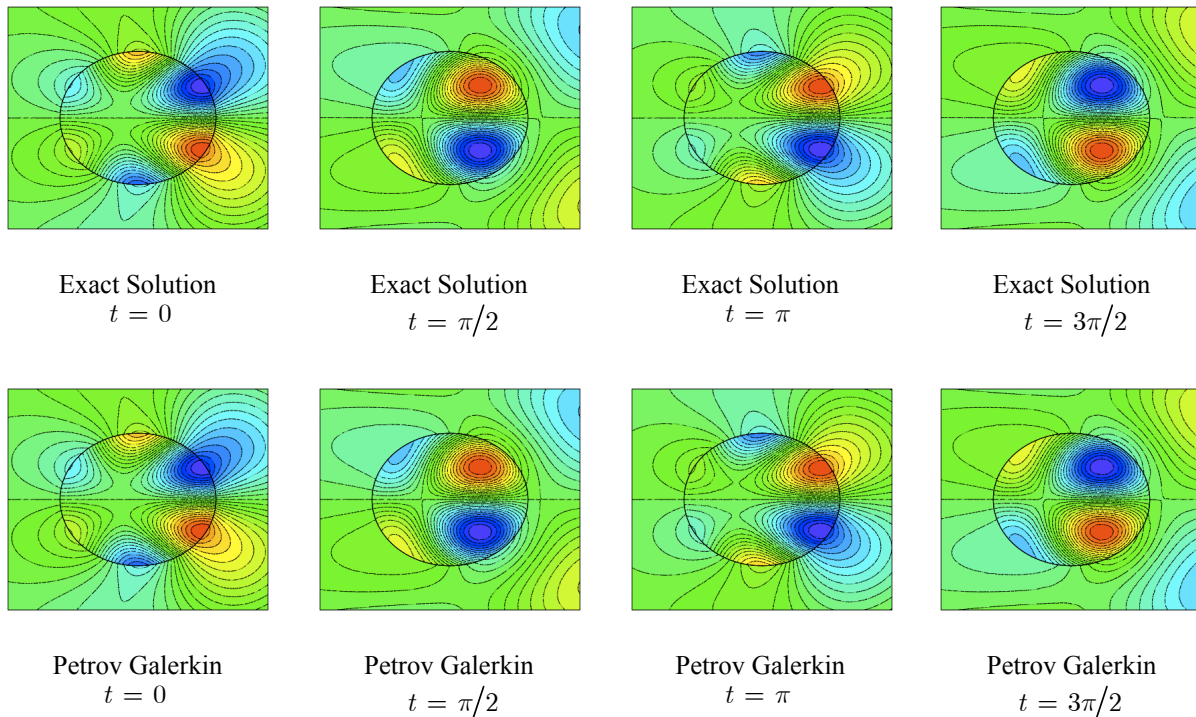| Petrov Galerkin $t = 0$ | Petrov Galerkin $t = \pi/2$ | Petrov Galerkin $t = \pi$ | Petrov Galerkin $t = 3\pi/2$ |

Figure 2. Comparison of Magnetic Flux Density Between Exact Solution and Petrov-Galerkin Method

Quantitative comparisons are shown in Tables 3-6 for both the PG and DG schemes using linear and quadratic elements. In the tables the L_1 and L_2 norms of the errors are given as well as the slopes indicating the order of spatial accuracy. For linear elements, given in Tables 3 and 4, it is seen that the errors in the L_1 norm between the PG and DG schemes are almost identical, whereas in the L_2 norm the errors associated with the PG scheme are approximately 70% higher than that of the DG scheme. As noted in the text accompanying Table 2, on a given mesh the number of degrees of freedom for the DG scheme is higher than that for the PG scheme. As a consequence, in the L_1 norm, which is a measure of global accuracy, the DG scheme does not compare favorably with the PG scheme because the errors are almost identical whereas the number of unknowns, and hence the amount of work required to obtain a solution, for the DG scheme is between five and six times that of the PG scheme. A similar conclusion can be made when comparing the errors in the L_2 norm, although the extra work involved in the DG scheme is somewhat mitigated by the lower errors.

A similar comparison is given in Tables 5 and 6 for the PG and DG schemes using quadratic elements. In this case, errors in the L_1 norm are again almost identical whereas the L_2 errors for the PG scheme are approximately 80% higher than for the DG scheme on the same mesh. As with linear elements, the DG scheme does not compare favorably with the PG scheme in the L_1 norm but performs somewhat better when considered in the L_2 norm. Note that while the PG scheme has been implemented using linear and quadratic elements, the DG scheme has also been implemented with elements as high as quartic and the design order of accuracy has been verified. Finally, while not shown, the divergence of the magnetic flux density has also been monitored and in all cases exhibits one order lower convergence rate when compared to the solution error. This behavior is consistent with theoretical estimates because derivatives typically converge at a rate one order less than solution variables.

Table 3. Accuracy Study for Petrov-Galerkin Scheme With Linear Elements				
Degrees of Freedom	L_1 Error	L_1 Slope	L_2 Error	L_2 Slope
369	2.528E-01		2.373E-01	
1348	5.998E-02	2.2209	5.599E-02	2.2289
5153	1.488E-02	2.0786	1.394E-02	2.0740

Table 4. Accuracy Study for Discontinuous-Galerkin Scheme With Linear Elements				
Degrees of Freedom	L_1 Error	L_1 Slope	L_2 Error	L_2 Slope
1824	2.534E-01		1.422E-01	
7314	6.001E-02	2.0740	3.353E-02	2.0800
29376	1.489E-02	2.0050	8.296E-03	2.0090

Table 5. Accuracy Study for Petrov-Galerkin Scheme With Quadratic Elements				
Degrees of Freedom	L_1 Error	L_1 Slope	L_2 Error	L_2 Slope
1345	1.029E-02		1.045E-02	
5133	1.226E-03	3.2834	1.205E-03	3.3350
20097	1.504E-04	3.1300	1.514E-04	3.0929

Table 6. Accuracy Study for Discontinuous-Galerkin Scheme With Quadratic Elements				
Degrees of Freedom	L_1 Error	L_1 Slope	L_2 Error	L_2 Slope
3648	1.002E-02		5.826E-03	
14628	1.198E-03	3.0590	6.692E-04	3.1160
58752	1.478E-04	3.0100	8.417E-05	2.9820

A comparison between the exact value of the y-component of the magnetic flux density and the simulations is shown in Fig. 3a, with a similar comparison for the z-component of electric flux density shown in Fig. 3b. The data is extracted along a line extending from the minimum x-coordinate to the maximum x-coordinate and passing through the center of the circle. Note that along this line and at this particular time, B_x is zero and is therefore not shown. As seen in the figures, the solutions obtained with the PG and DG schemes are in excellent agreement and are both indistinguishable from the exact solution. In particular, the jumps across the interface between the cylinder and the free stream are very accurately modeled, thereby confirming that the Riemann solver works well in this region.
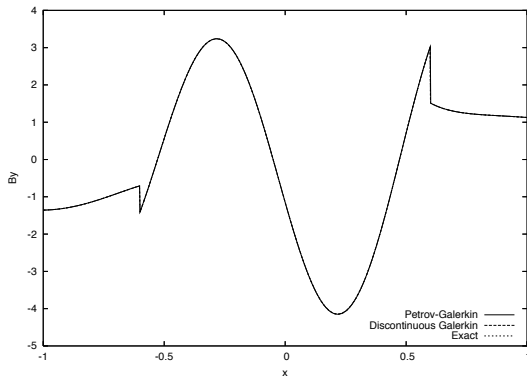
a) Y-Component of Magnetic Flux Density   b) Z-Component of Electric Flux Density
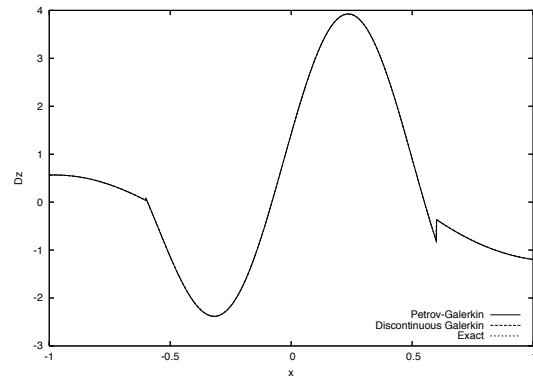
Figure 3. Comparison of Simulated Field Data with Exact Solution

Although the discretization of the spatial derivatives in the time- and frequency-domains is identical, a separate order-of-accuracy study has also been completed for a frequency-domain implementation of the Petrov-Galerkin scheme with results shown in Table 7. In the table, the rate of convergence in the L_1 norm for individual components of the field is given. As seen in the second column, linear elements provide second-order convergence for all the variables, as expected. Note that for linear elements, the geometry is modeled as a sequence of straight-line segments. When the same approximation is used for higher-order elements, the geometry is not reproduced to the same order-of-accuracy as the interior scheme because curvature is not properly taken into account. As seen in the table, the consequence of using a linear representation of the surface for quadratic elements is that the design order of accuracy is not obtained and is less than when linear elements are used. However, although not shown, the error levels for the nominally higher-order scheme are one order of magnitude less than for the linear scheme. As seen in the fourth column, by properly representing the surface to account for curvature, the design order of accuracy is achieved. While properly accounting for curvature is fairly trivial for simple geometries, such as cylinders, this presents a much more challenging task for complex geometries in three dimensions. To properly account for the curvature of the geometry requires close coupling between a computer aided design (CAD) model, the mesh generation, and the field solvers. An intermediate solution, albeit not very elegant, is to generate a highly refined representation of the surface and then "snap" all the nodes on the surface to the higher-fidelity representation. In the present work, this procedure is not followed for complex cases but will be implemented in the future.

	Table 7. Order of Accuracy of Petrov-Galerkin Scheme for Dielectric Cylinder		
	Frequency Domain		
	Linear	Quadratic (Linear Geometry)	Quadratic (Quadratic Geometry)
B_x	2.2181	2.0675	2.9667
B_y	2.3263	2.0546	3.0138
D_z	2.4441	2.0697	3.0666

In the previous section, exact solutions have been used to quantitatively determine the accuracy of the PG and DG schemes for a two-dimensional problem. In this section, qualitative results are obtained to test various aspects of the implementation. In Fig. 4, a frequency-domain solution for the dielectric cylinder is again considered, but instead of using exact data to drive the solution in the far field, eight PML regions are included to absorb outward moving waves, and the solution is driven using the Riemann solver described in connection with Eqs. 28 and 29. In this regard, the driving solution along the interfaces between the PML and the interior region is given by a simple propagating wave as described in Eqs. 30-32 [45].

$$B_x = 0 \tag{30}$$

$$B_y = -\cos\left(\omega\left(x - x_0\right)\right) - i\sin\left(\omega\left(x - x_0\right)\right) \tag{31}$$

$$D_z = \cos\left(\omega\left(x - x_0\right)\right) - i\sin\left(\omega\left(x - x_0\right)\right) \tag{32}$$

11

Figure 4 depicts contours of the real part of the x-component of magnetic flux density similar to that shown in Fig. 2. As seen, the contours obtained using the PG scheme agree qualitatively very well with the exact solution interpolated onto the same mesh, demonstrating that using the Riemann solver along the interfaces is effective at driving the correct solution. In particular, note that for the driving solution, the x-component of the magnetic flux density is zero and the direction of propagation, determined from the Poynting vector, is solely dependent on the y-component of the magnetic flux density and the z-component of the electric flux density. With the presence of the cylinder, clearly the x-component of the magnetic flux density is no longer zero and the final solution agrees well with the exact solution. Also shown in Fig. 4c is a far-field view of the domain where it is observed that the contours are continuous across the interfaces between the interior region and the PML regions, and that they vanish at the far-field boundary. By probing the contours in the far-field, all the variables, which represent deviations from the incoming wave, are all below negative 100 dB indicating that the PML is damping the outgoing waves very well.

| a) Exact Solution | b) Petrov-Galerkin Solution Quadratic Elements | c) Petrov-Galerkin Solution Entire Domain Including PML |
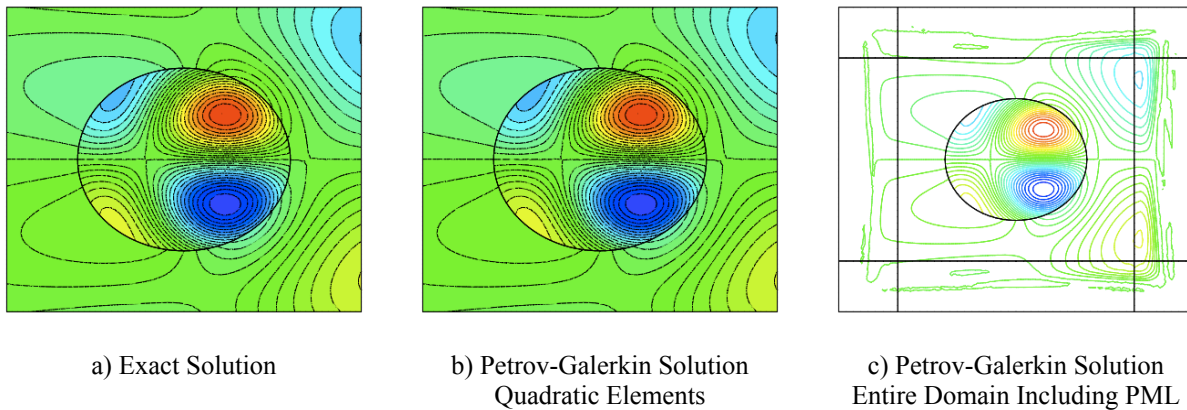
Figure 4. Frequency-Domain Solution for Dielectric Cylinder with Eight PML Regions in Far Field

A series of tests have been conducted comparing scattering parameters computed with the PG and DG codes with those obtained from a mode-matching formulation for an H-plane 2-pole iris band-pass filter [55-57]. This case is used to verify the procedure for computing scattering parameters, as well as further verification of the port boundary conditions and the PML implementation in the frequency domain. It should be noted that the mode-matching results are not exact solutions but provide useful comparisons with accepted methodologies for solving this type of problem.

The geometry for the filter is shown in Fig. 5a, providing the dimensions in millimeters, and clearly indicating that the geometry is slightly different between the upper and lower portions of the filter. A "baseline" mesh for the iris, consisting of 2,936 nodes, is shown in Fig. 5b, whereas Fig. 5c shows the mesh with PML regions on either end.

a) Dimensions for Geometry (mm)

b) Mesh for Band-Pass Filter

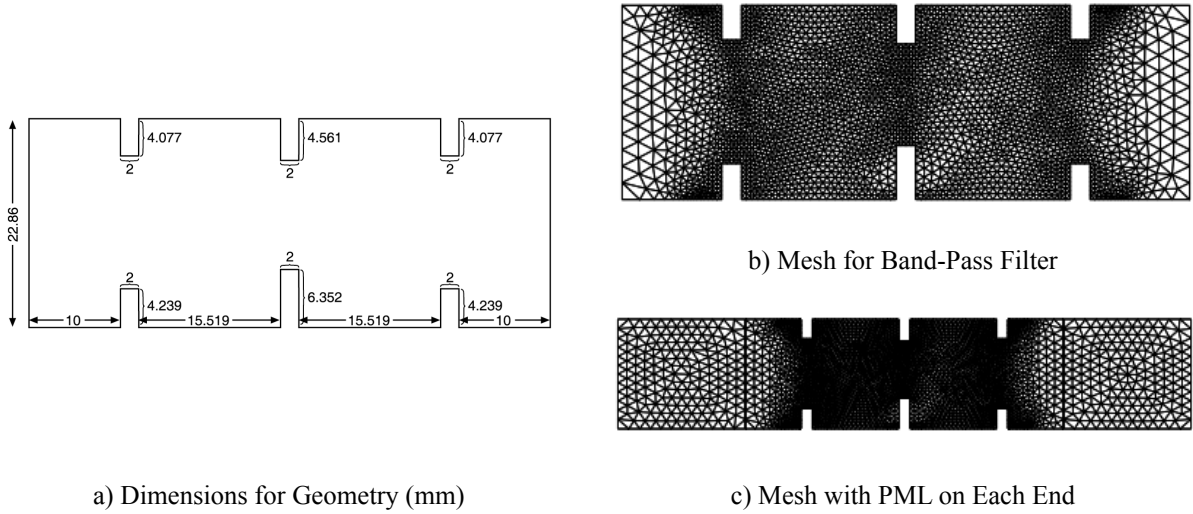

c) Mesh with PML on Each End

Figure 5. Geometry and Baseline Mesh for Two-Pole Iris Band-Pass Filter Simulation

For this simulation, a TE_{10} wave is used as the driving waveform in the Riemann solver at the interface between the left PML region and the filter. For calculating the scattering parameters, the time-average power is first computed on the interfaces between the PML regions and the iris

$$P_{reflected} = \frac{1}{2} \int \tilde{\boldsymbol{E}}_{reflected} \times \tilde{\boldsymbol{H}}^*_{reflected} d\Gamma \tag{33}$$

$$P_{incident} = \frac{1}{2} \int \tilde{\boldsymbol{E}}_{incident} \times \tilde{\boldsymbol{H}}^*_{incident} d\Gamma \tag{34}$$

Assuming an outward-pointing normal relative to the iris, the reflected variables correspond to those on the right side of the interface between the PML and the iris, whereas the incident values are obtained using those on the left side of the same interface after subtracting the reflected variables. Similarly, transmitted power can be obtained on the interface with the right PML where it should be noted that variables on either side of the interface can be used. After computing the time-average incident, reflected, and transmitted powers, the scattering parameters are computed as the square root of the ratio of the reflected power and transmitted power divided by the incident power [58].

$$S_{11} = \sqrt{\frac{P_{reflected}}{P_{incident}}} \tag{35}$$

$$S_{21} = \sqrt{\frac{P_{transmitted}}{P_{incident}}} \tag{36}$$

Figures 6a and 6b depict scattering parameters computed using the PG scheme with linear and quadratic elements, respectively. For the solution obtained with linear elements, a mesh consisting of 13,050 nodes (including the PML regions) has been used, whereas the comparable mesh for quadratic elements has only 3,315 nodes, which corresponds to 12,851 degrees of freedom. As seen, the agreement is very good across the frequency range between the present simulations and those obtained using mode-matching[55].
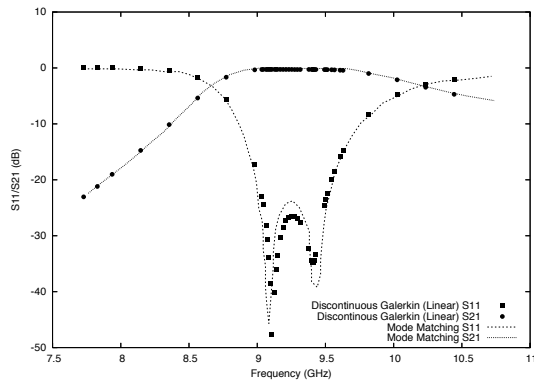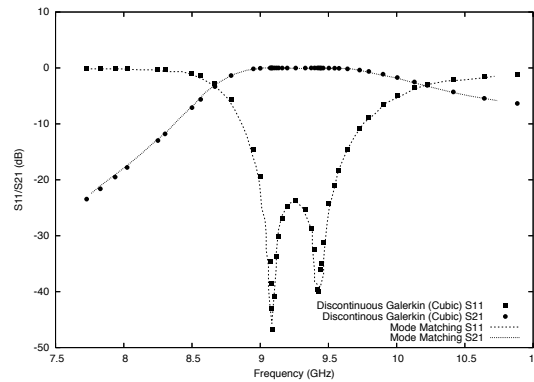
13
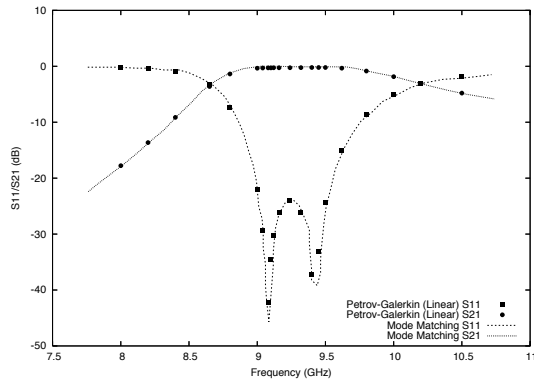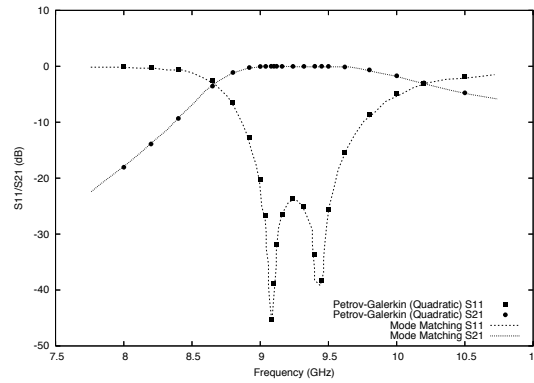
| a) Linear Elements | b) Quadratic Elements |

Figure 6. Scattering Parameters for Frequency-Domain Petrov-Galerkin Solution
Compared with Mode Matching [55]

Similar results are shown in Figs. 7a and 7b for the discontinuous-Galerkin scheme. It should be noted that the mesh used for these simulations is different from the meshes used above due to the difference in the number of degrees of freedom in the DG scheme compared to the PG scheme. The mesh used here has only 875 nodes and 1,544 triangles, which corresponds to 4,632 degrees of freedom for linear elements and 15,440 degrees of freedom for cubic elements. It should be noted that the purpose of this computation is not to provide a comparison with the PG scheme, but is intended to verify that the routine for computing the scattering parameters is correct and that the port boundary condition and PML each operate as expected. It is seen in the figures that the agreement between the DG solution and the mode-matching solution is good, although the linear elements show some slight discrepancies due to the coarseness of the mesh.

| a) Linear Elements | b) Cubic Elements |

Figure 7. Scattering Parameters for Frequency-Domain Discontinuous-Galerkin Solution
Compared with Mode Matching[55]

To examine the effect of mesh size on the PG solutions, simulations have been run using several mesh sizes and the scattering parameters are compared. Here, the time-domain version of the PG code has been used where a Gaussian pulse is used to excite the incoming wave and a Fourier transform of the field variables is accumulated

14

during the solution process for each of 150 evenly-spaced frequencies ranging between 7.5 and 11 GHz. In Fig. 8a, solutions on coarse (875 nodes), medium (3,315 nodes), and fine (13,050 nodes) meshes have been obtained using linear elements, where it should be noted that the number of nodes includes the PML regions. As seen, the solution with only 875 nodes is not particularly accurate but is steadily improved with mesh refinement, as expected. A similar plot for quadratic elements is shown for solutions on the 3,315 node mesh and the 875 node mesh, showing much less variation between the meshes due to the increased order of accuracy. Note that the minimum value of s_{11} occurring at about 9.5 GHz is not captured as well with the time-domain simulation as it is with the frequency-domain simulation, even though the spatial discretization of the schemes is identical. Because the PML effectively determines the boundary conditions for the problem, it is believed that the cause is attributable to the PML, which is implemented differently between the time-domain and frequency-domain codes. In the frequency domain, the PML is implemented by applying a stretching to the complex component of the coordinates for the regions in the PML[52, 53]. In contrast, the PML for the time-domain is implemented using an auxiliary equation as discussed in Ref. [53].

a) Linear Elements   b) Quadratic Elements
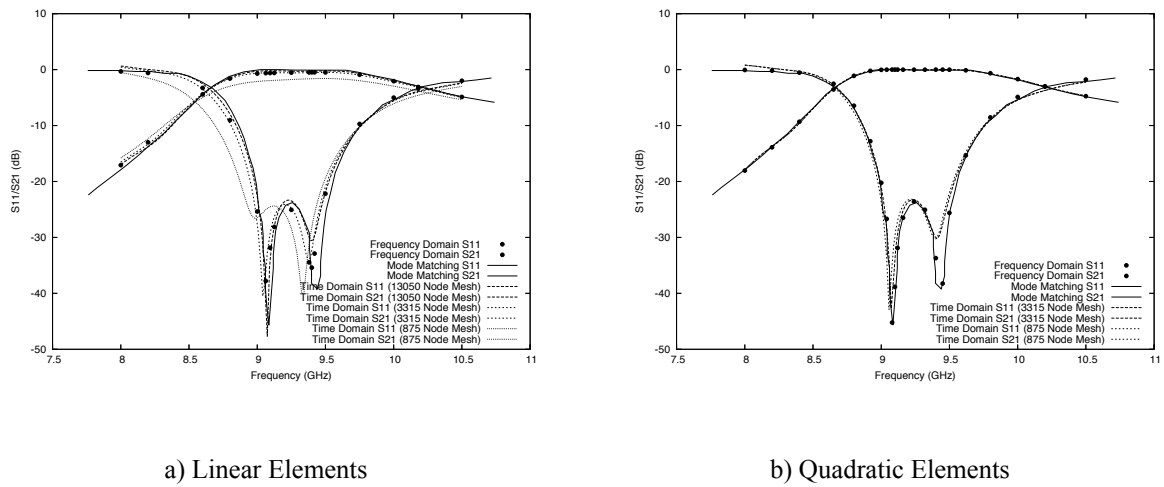
Figure 8. Grid Resolution Studies for Two-Pole Iris Band-Pass Filter with Petrov-Galerkin Scheme

A study to examine the sensitivity of the time-step size on the qualitative solution accuracy has also been conducted for the PG scheme with quadratic elements using the mesh with 3,315 nodes. The results, shown in Fig. 9a, indicate that the time-step variation ranging from 0.005 to 0.02 (nondimensionalized by speed of light and the height at the inlet) does not yield significant differences in the solution. In the previous solutions, a step size of 0.01 has been used, which is sufficiently small to have only a secondary effect on the scattering parameters.

As seen in Fig. 9b, a more pronounced effect on the solutions is seen by varying the loss coefficient associated with the PML, which determines how rapidly the solution is damped between the entrance to the PML and the end of the computational domain. It is obvious that a coefficient that is too small will reflect outgoing waves back into the interior of the mesh. However, as noted in Ref. [53], a coefficient that is too large will also cause reflected waves in a discrete implementation even though no reflections would be present in the continuous formulation. This effect is typically mitigated using a polynomial ramping function where the loss coefficient varies from zero at the entrance to the PML and reaches a maximum value at the end [53]. In this study, the maximum loss coefficient has been varied over a range between 15 and 250 and either a quadratic or quartic polynomial has been used. Although not shown, the differences precipitated by using the quadratic or quartic polynomial are much less than those observed by varying the maximum loss coefficient. As seen in Fig. 9b, a coefficient of 15 is clearly inadequate, while significantly less variation in the solutions is observed for coefficients greater than 50. For all the results previously shown, a loss coefficient of 50 has been used.
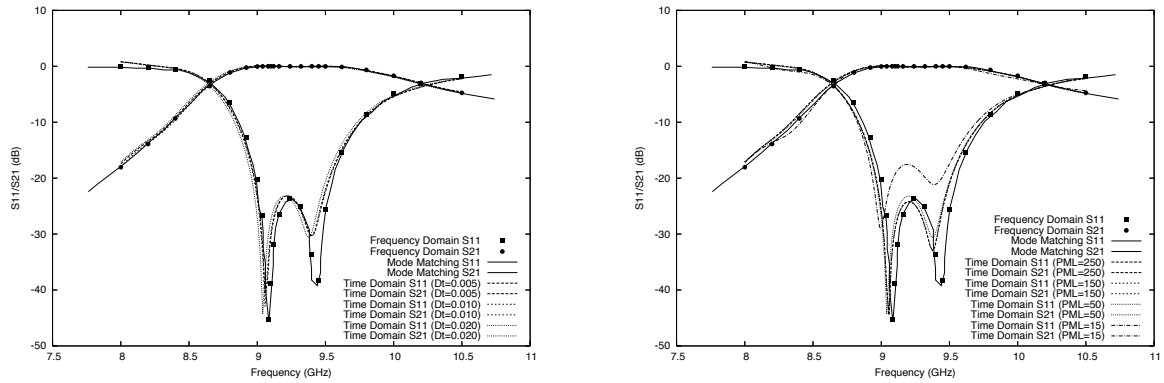
a) Effects of Time Step on Scattering Parameters   b) Effects of PML Coefficient on Scattering Parameters

Figure 9. Time-Step Size and PML Coefficient Studies for Petrov-Galerkin Scheme with Quadratic Elements

To determine whether the design order of accuracy is obtained for the three-dimensional PG and DG codes, an accuracy study has been conducted where the exact solution for a resonant cavity [59] is used for comparison. Figure 10 shows a comparison of solutions obtained using both the PG and DG schemes on the same mesh. In the figure, the x-component of the magnetic flux density from a time-domain solution is shown and is seen to be qualitatively the same between the two schemes. A quantitative comparison of the accuracy for each scheme is given in Fig. 11 where Fig. 11a shows a comparison between PG results and the exact solution and Fig. 11b shows similar results for the DG scheme. As seen in the figure, the accuracy of the PG and DG schemes are extremely close and are, in fact, the same within the first 3 decimal places. As expected due to the small differences in actual errors, the slopes of the L_1 norm of the error are the same between the two schemes. Furthermore, in both cases the design order of accuracy is achieved where a slope of 2.02 is obtained for linear elements and 3.09 for quadratic elements. Because the PG scheme appears to achieve similar error levels as the DG scheme but at lower cost, the majority of results presented henceforth are obtained with the PG finite-element formulation.
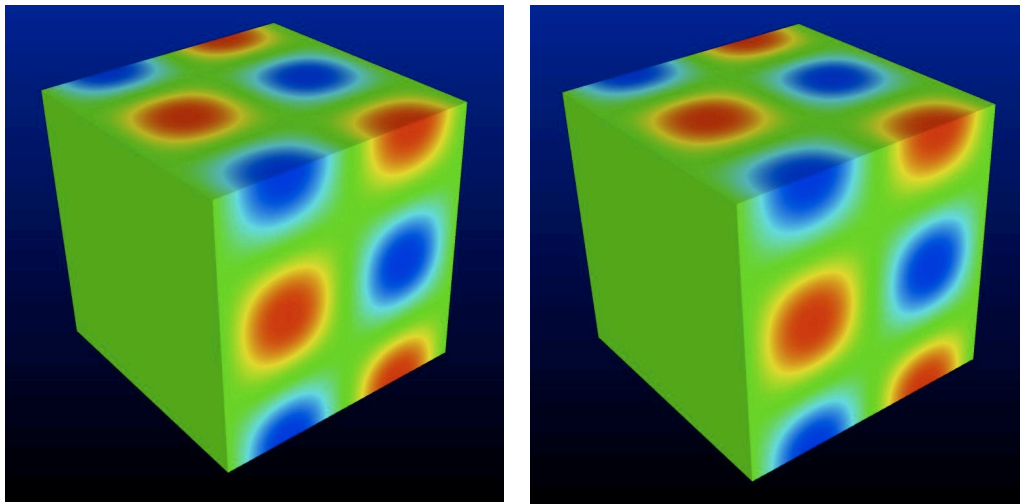
a) Petrov-Galerkin Solution   b) Discontinuous-Galerkin Solution

Figure 10. X-Component of Magnetic Flux Density using Petrov-Galerkin and
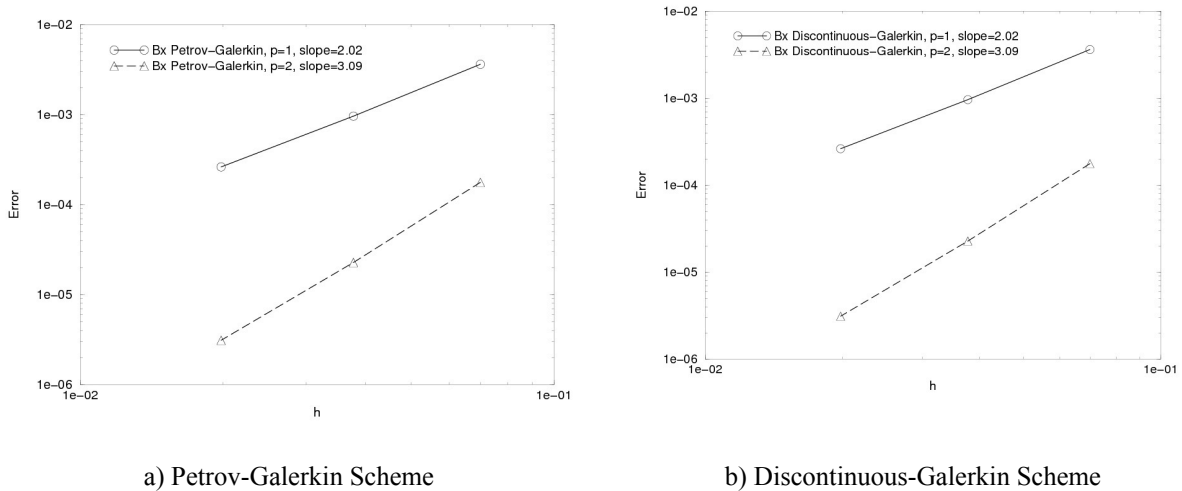Discontinuous-Galerkin Schemes for Resonant Cavity

a) Petrov-Galerkin Scheme   b) Discontinuous-Galerkin Scheme

Figure 11. Comparison of Order of Accuracy Between Petrov-Galerkin and Discontinuous-Galerkin Schemes for Resonant Cavity

Examination of Spurious Solutions

There has been a significant amount of literature on the occurrence and prevention of spurious solutions in electromagnetic simulations [60-63]. In the present formulation, the methodology is essentially the same used in many fluid dynamics applications involving inviscid compressible flow, whose equations have very similar mathematical structure. By providing appropriate dissipation through either the weighting term in the Petrov-Galerkin formulation, or through the Riemann solver in the discontinuous-Galerkin formulation, extensive regions of odd-even decoupling of solution values are precluded and spurious solutions are not expected. To verify this assertion, two-dimensional and three-dimensional tests have been conducted and the results are compared to accepted solutions. Results of these comparisons are shown in Figs. 12-14 while two examples of spurious solutions, taken from Refs. [63] and [64] are given in Fig. 15 for reference purposes.

The first test, described in Ref. [60] is for a circular cylinder divided into upper and lower halves, each with constant permittivity and permeability, but differing significantly between the two halves. In the upper half, the complex permittivity is given by $\varepsilon = 3 - i5$ and the permeability is 1.0. On the bottom half of the cylinder, both the permittivity and permeability are set to unity. For this case, the governing equations are the two-dimensional time-harmonic versions of Maxwell's equations assuming an electric field transverse to the z-direction.

$$i\omega\varepsilon\tilde{E}_x - \frac{\partial\tilde{H}_z}{\partial y} = 0 \tag{37}$$

$$i\omega\varepsilon\tilde{E}_y + \frac{\partial\tilde{H}_z}{\partial x} = 0 \tag{38}$$

$$i\omega\mu H_z + \frac{\partial\tilde{E}_y}{\partial x} - \frac{\partial\tilde{E}_x}{\partial y} = 0 \tag{39}$$

Contours of the real and imaginary parts of the magnetic field intensity are shown in Figs. 12a and 12b, respectively, from a Petrov-Galerkin solution using quadratic elements on a mesh with 804 nodes. Also shown in Fig. 12c are vectors formed from the real components of the electric field intensity. For comparison, similar results from Ref. [60] are shown in Figs. 13a-13c. As seen, the contours for both solutions are smooth and the vectors are

17

similar. In contrast, spurious solutions from Ref. [63] are shown in Fig. 15a, where the vectors are widely oscillatory and clearly do not satisfy the boundary conditions on the electric field that are required by the specification of $H_z = 1$ along this boundary. Specifically, the vectors on the outer boundary should be tangent to the boundary. This later observation is obtained by multiplying Eq. 37 by the x-component of a vector normal to the boundary and Eq. 38 by the y-component of the normal, adding them together, and noting that the tangential derivative of H_z is zero on the boundary. From the resulting equation, Eq. 40, it is apparent that the vector formed by the components of the electric field intensity on the outer boundary should all point in a direction tangent to the boundary. Clearly those in Fig. 15a do not.

$$i\omega\varepsilon\left(n_x E_x + n_y E_y\right) = n_x \frac{\partial H_z}{\partial y} - n_y \frac{\partial H_z}{\partial x} = 0 \tag{40}$$

a) Contours of Real(H_z)   b) Contours of Imag(H_z)   c) Vectors Formed using Real (E_x)and Real(E_y)
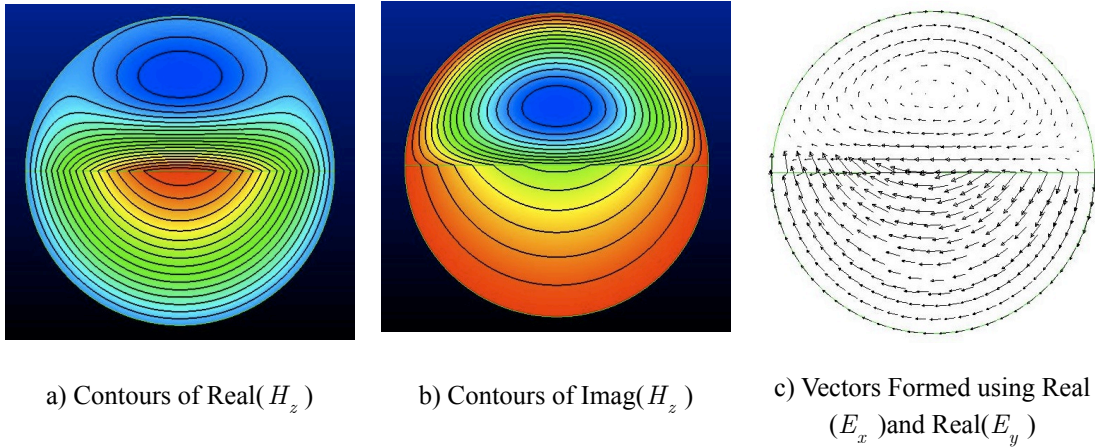
Figure 12. Petrov-Galerkin Solution for Split Cylinder

a) Contours of Real(H_z)   b) Contours of Imag(H_z)   c) Vectors Formed using Real (E_x) and Real(E_y)
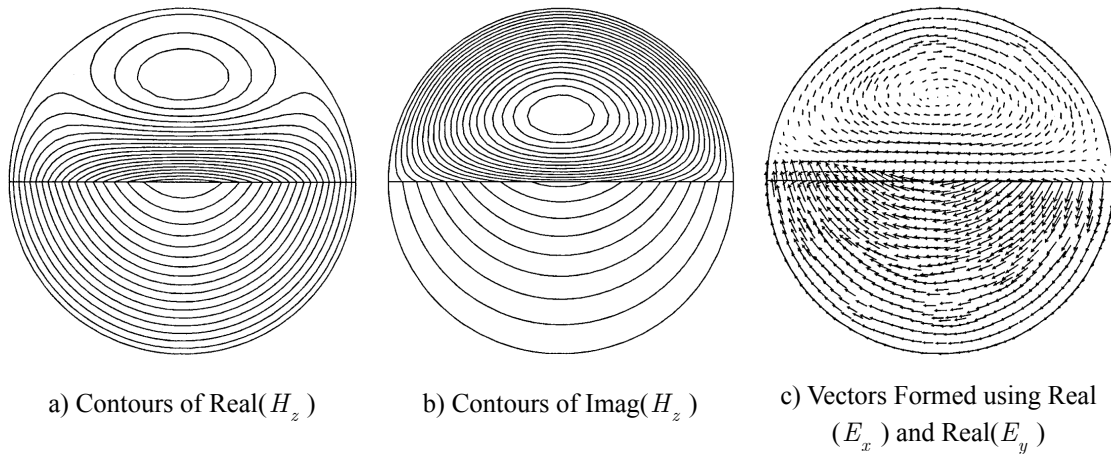
Figure 13. Solution for Split Cylinder From Reference [60]

18

For examining the presence or absence of spurious solutions in three dimensions, the case described by Ise [64] is considered. Referring to Fig. 14, a rectangular dielectric, with permittivity of 6.0 and permeability of 1.0, is placed inside a waveguide and the field is excited with a TE_{10} wave. The scattering parameters are then computed for several non-dimensional frequencies ranging between 1.6 and 2.6, and compared with existing solutions digitized from Ref. [64]. As seen in Fig. 14b, the scattering parameters are continuous over the frequency range and do not exhibit oscillations such as seen in Fig. 15b, which depicts spurious results also taken from Ref. [64]
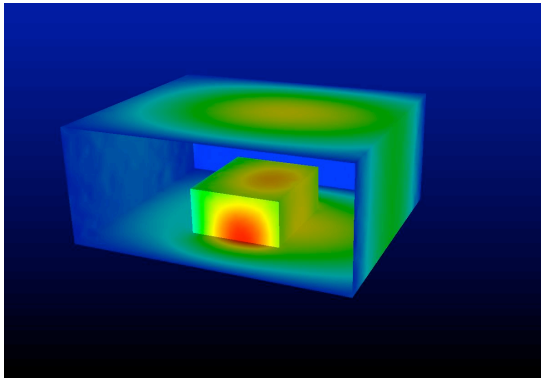
a) Real Part of x-Component of Magnetic Flux Density
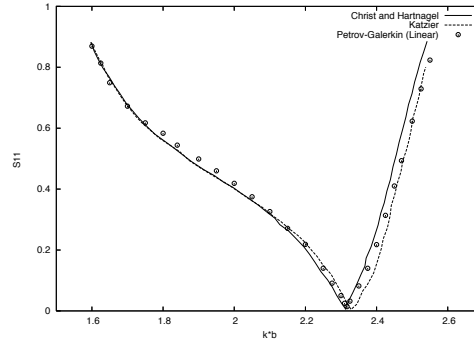
b) Scattering Parameter Compared with Results from Ref. [64]

Figure 14. Solution for Dielectric-Loaded Waveguide
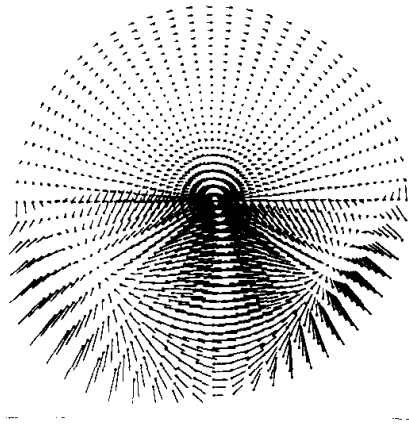
a) Spurious Solution for Split Cylinder from Ref. [63]
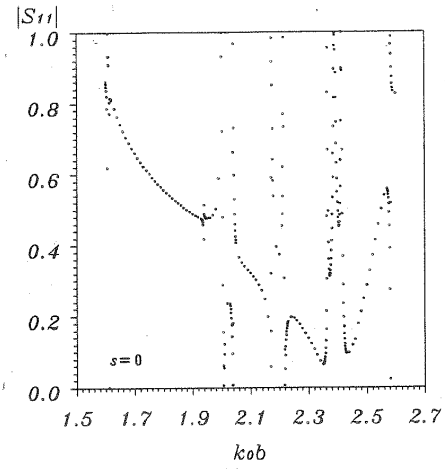
b) Spurious Solution for Dielectric-Loaded Waveguide from Ref. [64]

Figure 15. Examples of Spurious Solutions

19

Validation with Experimental Results

For validation purposes, the three-dimensional finite-element codes have been used to compute scattering parameters for a rectangular waveguide. Results are compared with experimental data [see volume 3 of this report] obtained with the intent of evaluating the ability of the simulations to predict changes in the scattering parameters caused by changes in geometric configurations or dielectric properties. A photograph of the experimental setup is shown in Fig. 16. In Fig. 16a, a waveguide under test is shown connected to an Agilent E8363B network analyzer, while Fig. 16b depicts a closeup view of the interior of the waveguide along with a protruding coax feed probe.

a) Network Analyzer and Waveguide   b) Interior of Waveguide Showing Coax Feed Probe
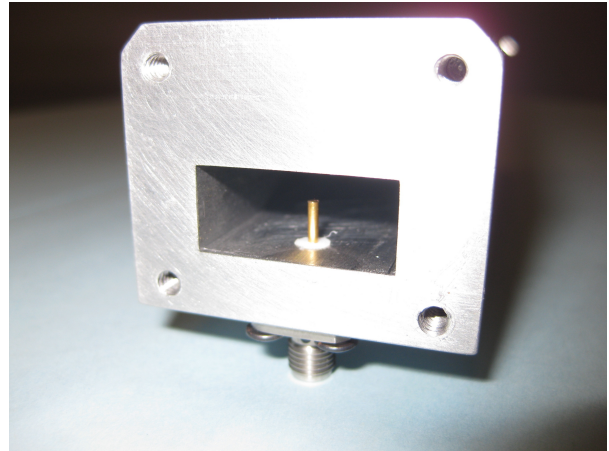
Figure 16. Experimental Setup for Obtaining Scattering Parameters for Waveguide Configurations

For all the experiments, a WR90 waveguide, with a 6-inch long interior cavity that is 0.9 inches wide and 0.4 inches high, is considered. Further details of the baseline geometry of the waveguide are given below in Fig. 17. Referring to Fig. 17a, it is apparent that the height of the interior of the waveguide is 0.4 inches and the length is 6 inches. Further, it is seen that the thickness of the lower wall is 0.315 inches. The feed probe is an Amphenol 901-9204-CCSF connector with the dielectric surface flush with the lower wall of the waveguide and the pin protruding 0.2 inches above the surface. The end view of the waveguide, shown in Fig. 17b, illustrates that the outer diameter of the feed probe is 0.162 inches, whereas the inner pin diameter is 0.05 inches. As shown in Fig. 17c, the inner pin is displaced 0.25 inches from the end wall and 0.45 inches from the side wall.

a) Side View

b) End View
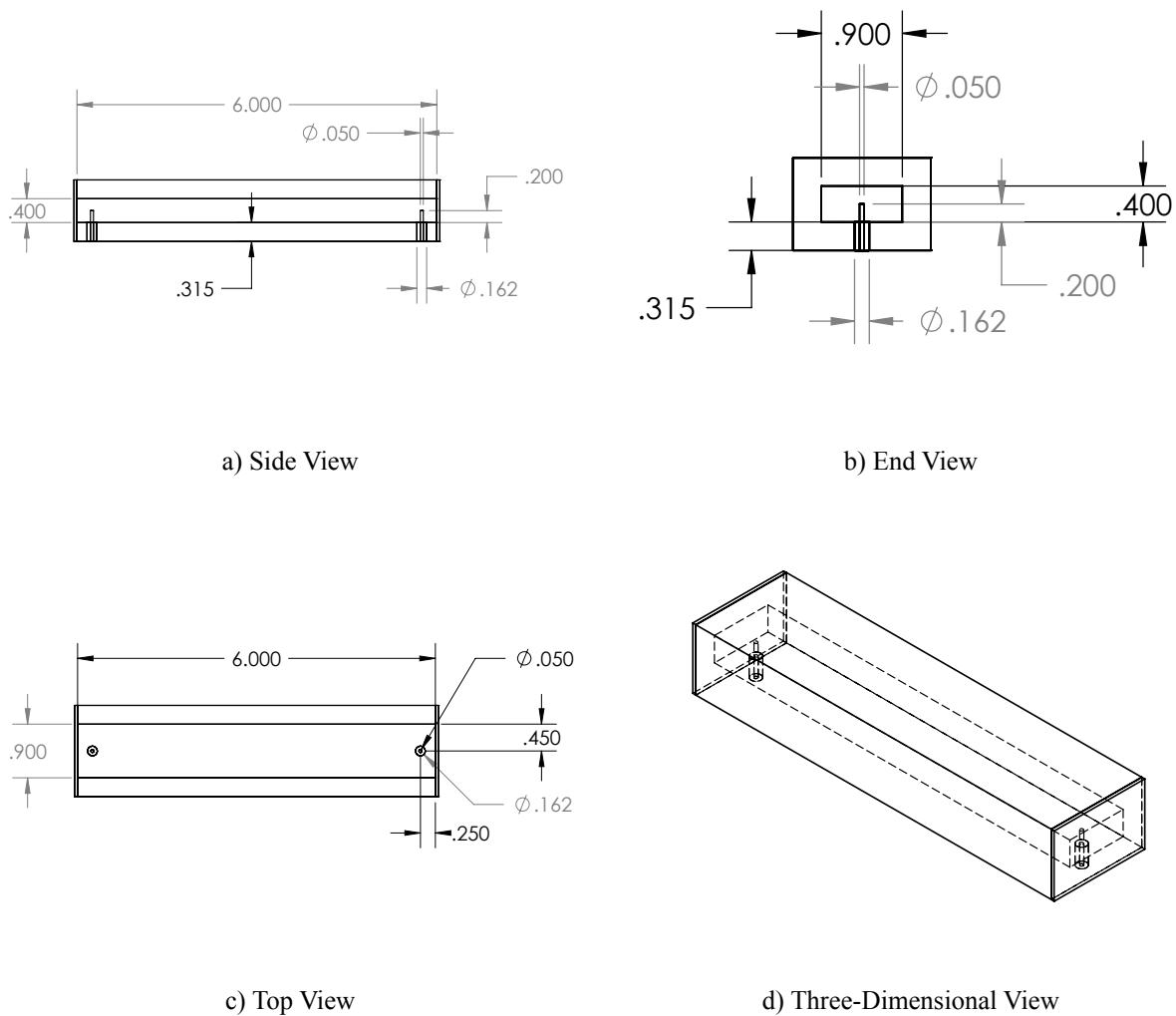
c) Top View

d) Three-Dimensional View

Figure 17. Geometry for Experimental Waveguide with Coax Feed Probe

During the experimental program, numerous variations from the baseline configuration have been considered. These variations include the displacement of the feed probe from the walls, changing pin height, and insertion of a dielectric that can be further configured by differing the geometry and relative dielectric constants. While not all combinations considered in the experimental program are used for validation purposes, results are shown below for the baseline case, as well as a case with the feed probe displaced from the end wall, and three cases with a dielectric insert.

An initial mesh for the baseline geometry consisting of 9,860 nodes and 45,315 tetrahedra is depicted in Fig 18. In this mesh approximately 30 nodes are distributed along the length of the waveguide with 10 points across the width, thereby providing roughly 5 points per wavelength based on a maximum frequency of 12 GHz. Figure 18a shows an overall view of the mesh where the body of the waveguide is depicted in green, the portions of the coax cable within the thickness of the lower wall in red, and a short piece of coax extending out of each end of the waveguide are shown in yellow and blue. Similarly, a close-up view of the mesh in the proximity of the coax feed probe is shown in Fig. 18b, where the dielectric is shown in white and the center pin in orange.
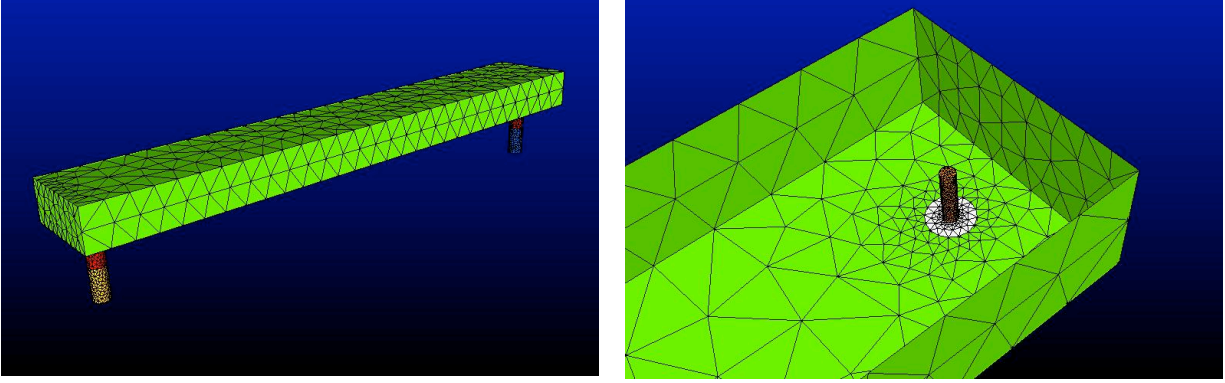
a) Far-Field View   b) Closeup View Near Coax

Figure 18. Initial Mesh for Baseline Case

Perfect electric conducting (PEC) boundary conditions are used on the walls of the waveguide, as well as on the shielding and pin portions of the coax. Duplicate nodes are created along the interfaces between the dielectrics and air-filled regions of the waveguide, and the Riemann solver is used to resolve the flux integral across these boundaries. Note that the dependent variables on either side of the interfaces represent full-wave components of the field variables and are obtained as the solution evolves. The relative permittivities of the dielectric material and the internal portion of the waveguide are given by 2.1 and 1.0, respectively; the permeability is 1.0 for all regions. The coax cables extending from the waveguide are terminated with a PML [52] for frequency-domain simulations and Silver-Muller boundary conditions [65] for time-domain simulations. This later boundary condition should be applicable in this region because the transverse electric magnetic (TEM) nature of a coax facilitates a wave traveling normal to this boundary. Excitation of the field is achieved by creating duplicate faces and using the Riemann solver at the interface between the coax cable normally interior to the waveguide (red) and that portion protruding outward (yellow). Here, the driving field components used in Eqs. 28 and 29 are determined using the exact solution for a coax given by [58]

$$\tilde{E}_x = -\frac{V_0}{\ln(b/a)} \frac{(x - x_0)}{r^2} \tag{41}$$

$$\tilde{E}_y = -\frac{V_0}{\ln(b/a)} \frac{(y - y_0)}{r^2} \tag{42}$$

$$\tilde{E}_z = 0 \tag{43}$$

$$\tilde{H}_x = -\frac{1}{\eta} \tilde{E}_y \tag{44}$$

$$\tilde{H}_y = \frac{1}{\eta} \tilde{E}_x \tag{45}$$

$$\tilde{H}_z = 0 \tag{46}$$

Here, note that a and b correspond to the radius of the pin and feed probe, respectively, whereas r is the local radius at a given mesh point.

Solutions for the baseline configuration obtained using the Petrov-Galerkin scheme with quadratic elements are shown in Fig. 19. Contours of the x-component of the magnetic flux density are shown in Fig. 19a, for a frequency-

domain solution at approximately 10 GHz, whereas Fig. 19b shows scattering parameters across a range of frequencies, computed using both the frequency-domain and time-domain versions of the codes. The frequency-domain solutions have been obtained through a series of independent simulations obtained at each frequency with the results shown as symbols in the figure. For the time-domain results, scattering parameters are obtained for 150 evenly-spaced frequencies in a single run by applying a Gaussian pulse to the driving fields and computing the Fourier transforms of the solution variables along the duplicate faces. The time-averaged incident, reflected, and transmitted powers are then computed from which the scattering parameters are then derived.

The contours shown in Fig.19a, clearly exhibit a discontinuity at the driving interface. The red contours illustrate the traveling wave whereas the lack of color in the PML region demonstrates that there is very little reflected power at this particular frequency.

Scattering parameters obtained from the simulations using quadratic elements are compared with experimental data in Fig. 19b and demonstrate that both the frequency-domain and time-domain solutions agree well with each other as well as with experiment. Note that scattering parameters are obtained for the time-domain simulations at many more frequencies than for the frequency-domain code. Further, while 150 frequencies are used for the present time-domain results, data at additional frequencies adds negligible cost to the simulations. This is because each frequency only requires a Fourier transform computation along the interface regions where the scattering parameters are computed, which represents a very small subset of the overall mesh. Although the savings in computer time derived from using the time domain depends on the number of frequencies considered, it is clear that the time-domain approach can be much more efficient than the frequency-domain approach for this problem. This is especially true when one considers that the time-domain solution reveals the nature of the scattering parameters across the entire frequency range in a single run whereas the same information must be incrementally extracted using the frequency-domain approach. In addition, in the time-domain, diagonal dominance is typically achieved due to the time-step contribution making this approach somewhat more reliable in practice.
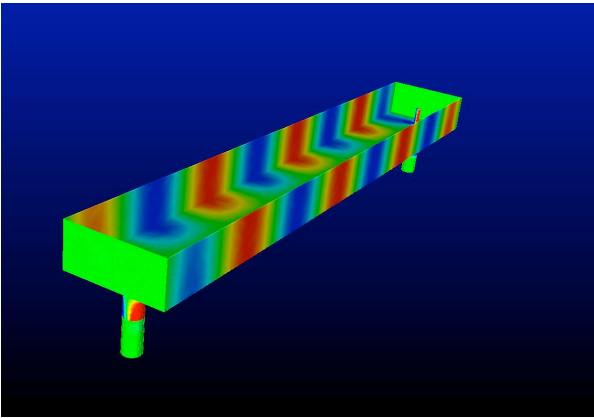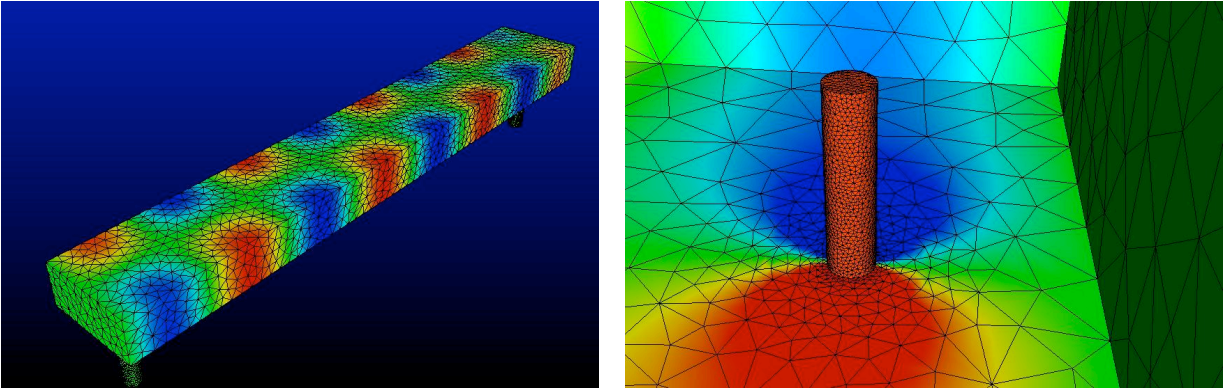

a) Real Part of x-Component of Magnetic Flux Density
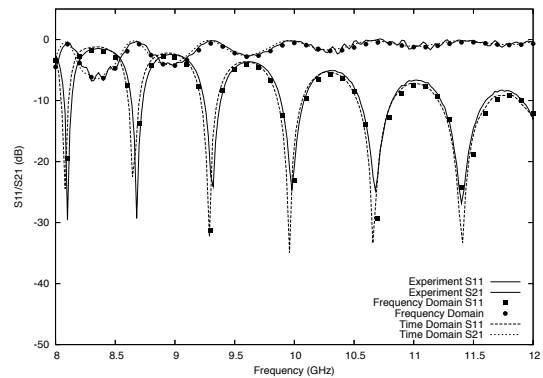
b) Comparison of Frequency-Domain and Time-Domain Scattering Parameters with Experiment

Figure 19. Comparison of Scattering Parameters Obtained From Simulations On Baseline Mesh with Experimental Data

To examine the effect on the computed scattering parameters caused by spatial discretization errors, a refined mesh is used where the number of points in each direction is increased by roughly 70%. The resulting mesh, depicted in Fig. 20, consists of 50,058 nodes and 246,852 elements and is clearly higher resolution compared to the initial mesh shown previously in Fig. 18.

a) Far-Field View

b) Closeup View Near Coax

Figure 20. Refined Mesh for Baseline Case and Contours of x-Component of Magnetic Flux Density Computed using Petrov-Galerkin Scheme with Quadratic Elements

Scattering parameters computed on this mesh using the time-domain formulation of the Petrov-Galerkin code with quadratic elements are shown in Fig. 21 below. Also shown on the figure are the previous results obtained on the initial mesh, as well as the experimental data. Only small differences are observed between the solutions on the initial and refined mesh with the primary difference being slightly less reflected power on the refined mesh as exhibited by the lower minimum values of S_{11}. Because the scattering parameters obtained on the finer mesh do not change appreciably from those on the initial mesh, the majority of the following simulations will be conducted on meshes that are derived from the initial mesh and therefore have a similar number of points.
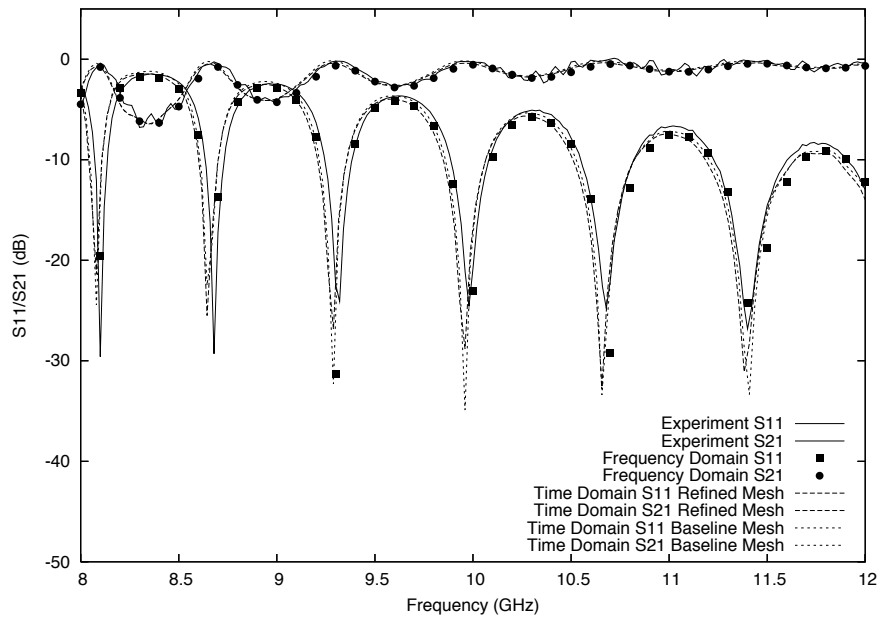

Figure 21. Scattering Parameters Computed on Baseline and Refined Mesh

It should be noted that on the initial mesh using the PG scheme with quadratic elements, there are approximately 78,880 degrees of freedom. To obtain a reasonable comparison in accuracy obtained using quadratic and linear elements, an additional mesh has been generated by refining the initial mesh by approximately a factor of two in all directions. The resulting mesh has 83,208 nodes and 431,590 tetrahedron. Because the number of degrees of freedom for linear elements is approximately the same as that for the initial mesh with quadratic elements, a direct comparison can be made between the schemes to demonstrate the benefits of the higher-order formulation. Results are shown in Fig. 22 depicting the scattering parameters obtained from frequency-domain and time-domain solutions using quadratic elements on the baseline mesh as well as time-domain results obtained using linear elements on the larger 83,208 node mesh. For a fair comparison between the accuracy obtained using the linear and quadratic elements, it should be emphasized that the terminology "refined mesh" in the figure is referring to the newly generated mesh and not the 50,058 node mesh previously discussed. As seen in the figure, although the larger mesh used with the linear elements contains slightly more degrees of freedom than when using quadratic elements on the initial mesh, the solution obtained using linear elements is noticeably inferior, thereby demonstrating the benefits of the higher-order formulation. In the remaining results, only results with quadratic elements are considered.
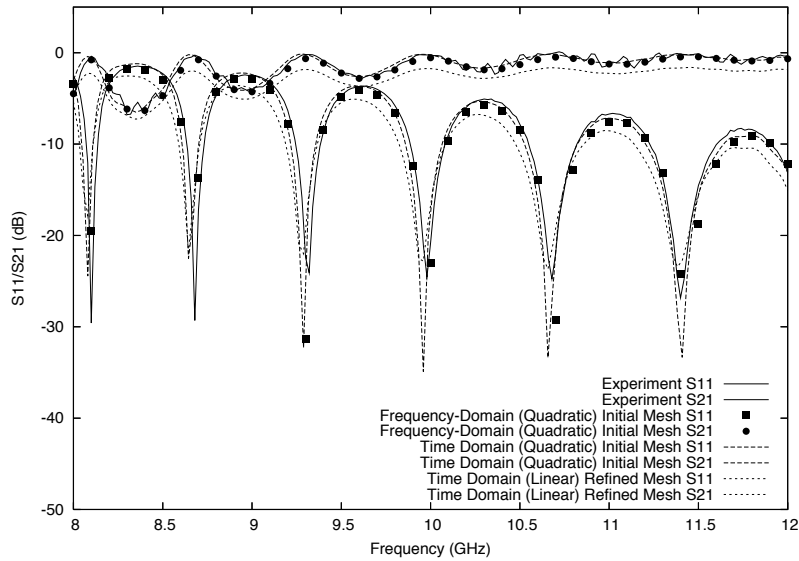

Figure 22. Comparison Between Petrov-Galerkin Results Obtained with Linear and
Quadratic Elements

The ability to successfully simulate changes in scattering parameters associated with variations from the baseline geometry has been evaluated, with the results shown in Figs. 23-27. The first deviation from the baseline geometry is obtained by shifting the position of the feed probe inward an additional 0.5 inches resulting in a final displacement of 0.75 inches from the end wall. The modified position of the feed probe is evident in Fig. 23a, which also shows contours of the real part of the x-component of the magnetic flux density obtained from a frequency-domain solution at 11 GHz. A comparison of simulated and experimentally determined scattering parameters is shown in Fig. 23b, where results are included from both time- and frequency-domain Petrov-Galerkin formulations with quadratic elements on a mesh with 15,648 nodes. As seen in the figure, the scattering parameters exhibit marked differences from those of the baseline geometry with small reflected power only occurring at about 10.25 GHz. As also seen in the figure, the time-domain and frequency-domain solutions are in excellent agreement with each other as well as with the experimental data.
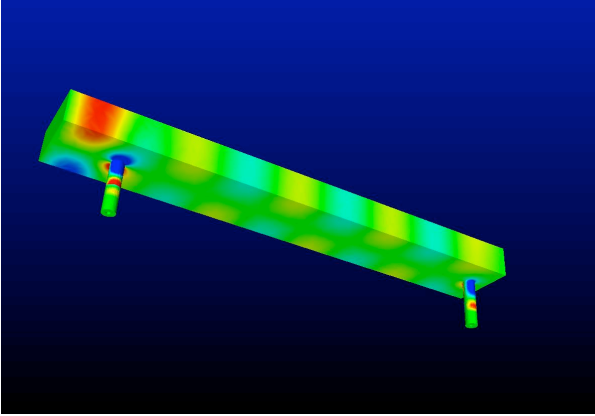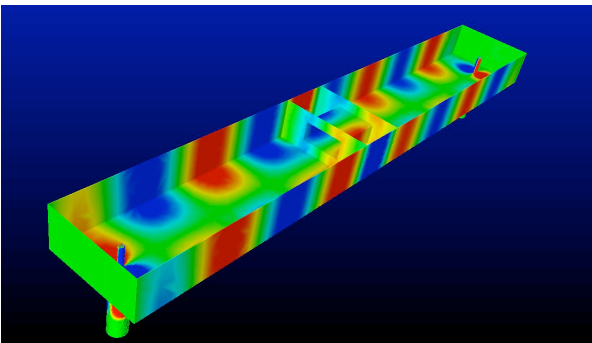
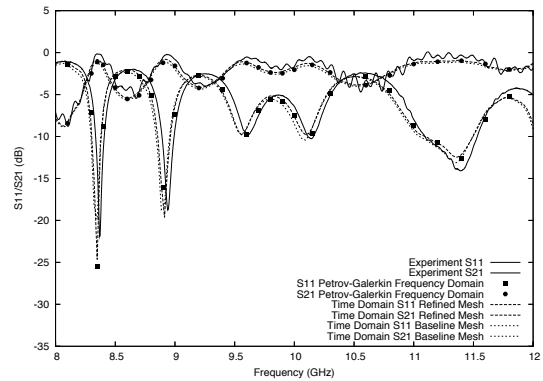a) Real Part of x-Component of Magnetic Flux Density
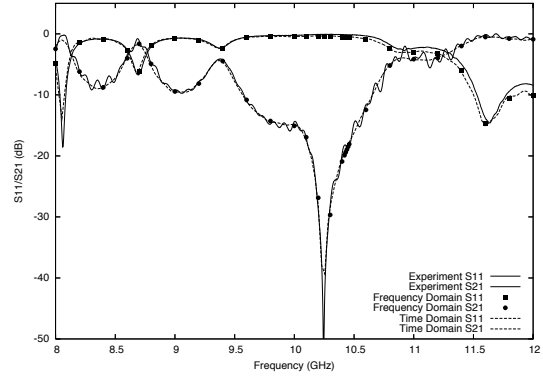
b) Comparison of Frequency-Domain and Time-Domain Scattering Parameters with Experiment

Figure 23. Comparison of Scattering Parameters Obtained From Simulations For Translated Coax Feed Probe

In the experimental program, several dielectric inserts of varying geometry and permittivity have been placed inside the waveguide 3 inches from the end wall closest to the feed probe. One of the dielectrics is 0.5 inches thick, spanning the entire width and height of the waveguide, and including a 0.4 x 0.2 inch rectangular hole through the material. Contours of magnetic flux density for this configuration are shown in Fig. 24a for an initial mesh comprised of 10,754 nodes and 49,490 tetrahedron. Here, the top of both the waveguide and the dielectric have been removed to clarify the geometry. It should be noted that while the interior of the waveguide is hollow, the dielectric is solid. As seen in Fig. 24b, the scattering parameters are consistent between the frequency-domain and time-domain solutions. For this geometry, a time-domain solution on a refined mesh, with 96,626 nodes and 514,971 tetrahedra, has also been obtained because of the extra complexity of the dielectric. As seen in the figure, there is no significant change in the scattering parameters on the finer mesh. Recalling that Silver-Muller boundary conditions are used for the time-domain solution whereas PML regions are used for the frequency-domain, it should be noted that a precise agreement between the solutions is not expected because of variations in the boundary conditions. Nevertheless, the consistency of results between the simulations and with the experimental data is very good.

a) Real Part of x-Component of Magnetic Flux Density

b) Comparison of Frequency-Domain and Time-Domain Scattering Parameters with Experiment

Figure 24. Comparison of Scattering Parameters Obtained From Simulations For Dielectric-Loaded Waveguide with Relative Permittivity of 4.0

Scattering parameters computed with the time-domain discontinuous-Galerkin code using quadratic elements are presented in Fig. 25. Experimental results are also shown, as are frequency-domain results obtained using the Petrov-Galerkin code. Cross-referencing the PG results with those in Fig. 24, it is also observed that close agreement with the time-domain PG code is also achieved. Note that using the estimates from Table 1, there are approximately 86,032 degrees of freedom for the PG code with quadratic elements, whereas there are approximately 494,900 degrees of freedom for the DG scheme discretized using the same order polynomial. A coarser initial mesh may be more appropriate for the DG scheme so the number of degrees of freedom is more consistent. However, this is somewhat complicated because of the linear representation of the geometry, which necessitates significantly more points in the surface definition than would be required if a quadratic definition is used. Coarsening the initial mesh is therefore difficult without losing the geometry. Properly accounting for the curvature in the coax cables could significantly reduce the degrees of freedom in both the PG and DG schemes.
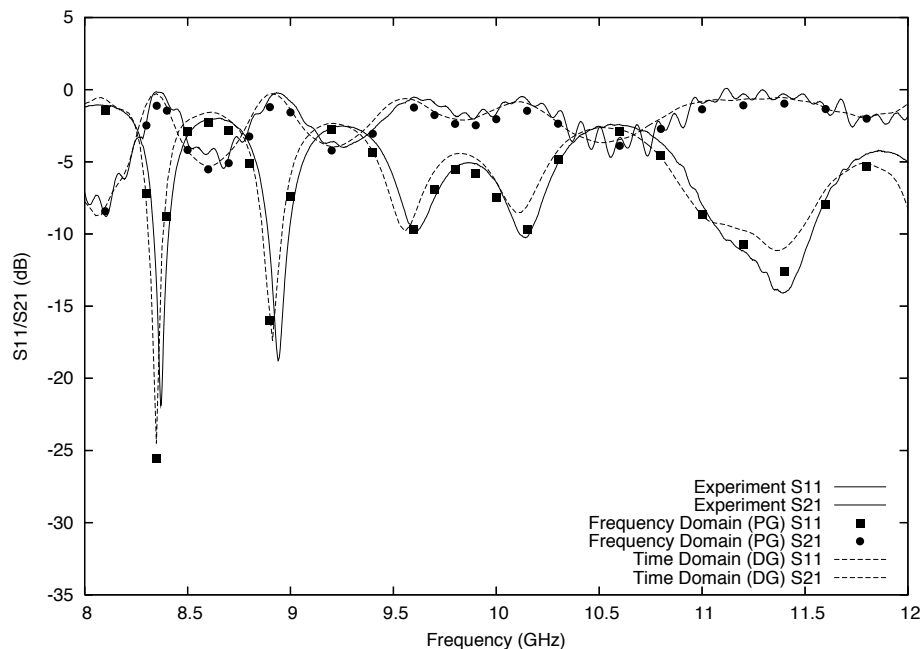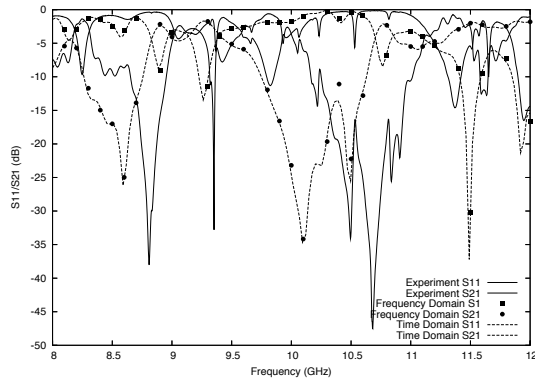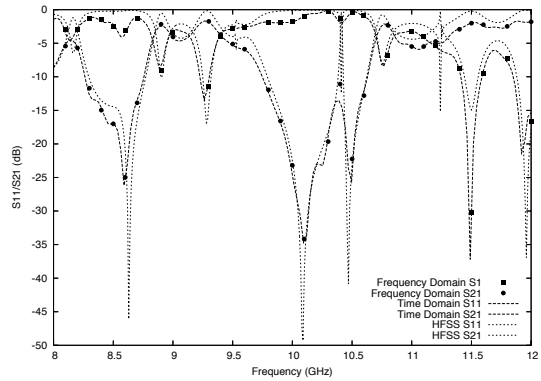

Figure 25. Comparison of Scattering Parameters Obtained From Frequency-Domain
Petrov-Galerkin Method and Time-Domain Discontinuous-Galerkin Method
Dielectric-Loaded Waveguide with Relative Permittivity of 4.0

Experimental data has also been obtained for the same dielectric but with a relative permittivity of 12.0. Fig. 26 compares experimental results with those of time-domain and frequency-domain results obtained using the PG formulation with quadratic elements. As seen, the simulations do not exhibit good agreement with experimental data for this case. One possible explanation is that visual inspection of the dielectric installed in the waveguide reveals that small gaps are present between the dielectric and the waveguide; however this explanation would not account for the good agreement seen with the dielectric with lower permittivity. However, the results from the Petrov-Galerkin code can by cross-checked with a well established commercial electromagnetic solver as a consistency check between the simulations. Figure 26b shows the results of this comparison where the commercial code HFSS [66] has been used. It is seen that the agreement between the simulation codes is very good so that it is believed that an undetermined inconsistency exists between the experimental and simulation setups.

a) Comparison of Petrov-Galerkin Scattering
Parameters with Experimental Data

b) Comparison of Petrov-Galerkin Scattering
Parameters with HFSS

Figure 26. Comparison of Scattering Parameters Obtained From Simulations For Dielectric-Loaded Waveguide
with Relative Permittivity of 12.0

As a final test case for evaluating the accuracy of the simulation codes, a "half-slab" dielectric with relative permeability of 4.0 is placed on its side 3 inches from the   end wall closest to the feed probe. Contours of the magnetic flux density are shown in Fig. 27, where the presence and orientation of the dielectric are clearly displayed. Scattering parameters, obtained using the PG algorithm with quadratic elements on a mesh with 10,716 nodes, are compared to experiment and with HFSS in figure 27b. It is seen in the figure that the simulations agree well with one another but that there are some noticeable differences in the comparison with experiment, particularly between 9.5 and 11.5 GHz.
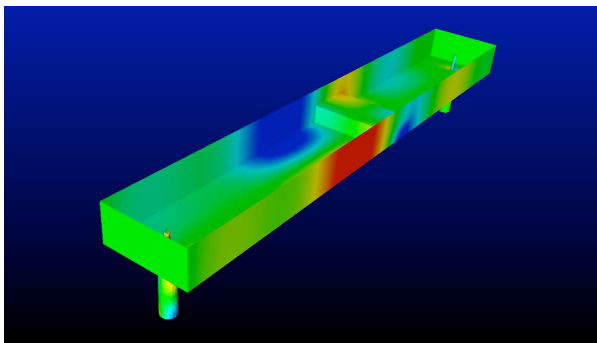

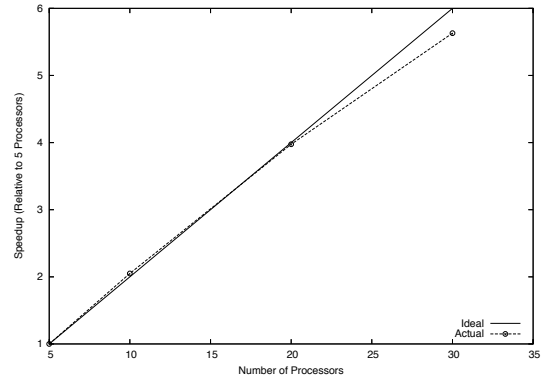a) Real Part of x-Component of Magnetic Flux Density
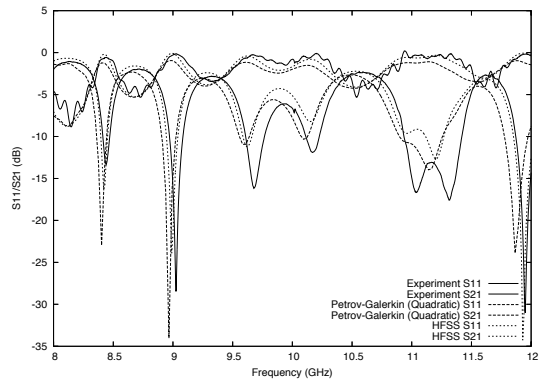
b) Comparison of Time-Domain Scattering Parameters
with HFSS and Experiment

Figure 27. Comparison of Experimentally Obtained Scattering Parameters with Simulations For Dielectric-Half-
Slab Loaded Waveguide: Relative Permittivity of 4.0

28

One objective in the development of the solvers is that good performance can be obtained in a parallel computing environment. The current codes have been developed on an IBM compute server with four eight-core IBM POWER7 3.55 GHz processors and 128GB of RAM. Figure 28a depicts the initial mesh for the baseline waveguide partitioned into 10 domains. The partitioning software described in Ref. [67] has been used for subdividing the mesh and the MPI message passing interface is used for communication among processors. As shown in Fig. 28b, 95% scaling is achieved on 30 processors with only a slight drop off caused by the fact that the initial mesh, partitioned into 30 domains, does not provide adequate work for each processor when compared to the communication cost. While larger meshes may be used on more processors, this will be pursued in the future where special emphasis will be placed on preparation to run on "leadership class" machines.
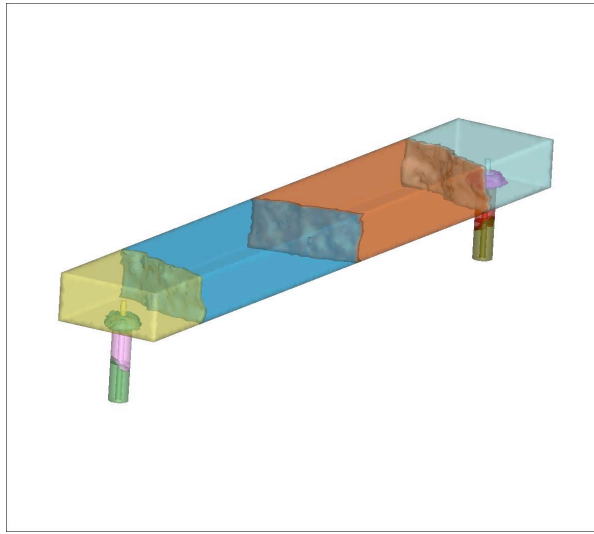
a) Example Partitioning into Ten Domains   b) Parallel Scaling

Figure 28. Parallel Scaling for Frequency-Domain Petrov-Galerkin Scheme on Baseline Mesh

Summary

High-order Petrov-Galerkin (PG) and discontinuous-Galerkin (DG) finite-element algorithms for solving Maxwell's equations have been developed for both time-domain and frequency-domain applications. For time-dependent applications, a fully implicit time-stepping algorithm is used that allows the time-step size to be determined by accuracy considerations and not by limitations typically imposed by explicit methods. The algorithms can be used to accurately model geometrically complex domains containing multiple materials of differing electromagnetic properties.

Verification tests for two- and three-dimensional applications have been conducted to examine the order of accuracy of the resulting schemes. Here, it is demonstrated that in the L_1 norm, both the PG and DG schemes achieve very similar levels of error on a given mesh whereas in the L_2 norm, the DG scheme demonstrates errors about 70-80% lower than those of the PG scheme. However, when considering the number of degrees of freedom, the PG scheme provides the same global accuracy as the DG scheme but with lower computational cost. For both the L_1 and L_2 norms, both schemes exhibit the design order of accuracy.

During the order-of-accuracy studies, it has been demonstrated that while the geometry can be modeled much more accurately than with a typical FDTD code, to truly obtain the design order of accuracy requires that curvature must be properly accounted for. While this can be handled for simple geometries, an integrated approach between computer aided design (CAD), mesh generation, and the solvers is recommended. Although the higher-order codes still demonstrate greater accuracy than the lower-order codes, even without properly accounting for curvature, the full potential of higher-order methods will only be achieved by addressing this issue.

Comparisons have been made between simulations and experimental data for a rectangular waveguide. Here, numerous geometric variations have been systematically altered to examine the ability of the codes to successfully predict accompanying changes in scattering parameters. Some variations include a dielectric insert placed within the waveguide, where the geometry and relative permittivity of the dielectric are both configurable. The benefits of the higher-order formulation is demonstrated and in all but one case the simulation codes successfully predict trends caused by varying these parameters. For the experimental case with a relative dielectric constant of 12.0, the scattering parameters obtained from the simulations do not demonstrate results consistent with the experiment. However, comparisons made with the commercial code HFSS show consistency between the simulations. The reason for the discrepancy in the experimental data for this case is unknown.

Bibliography

1.   Yee, K. S., "Numerical Solution of Initial Boundary Value Problem Involving Maxwell's Equations in Isotropic Media," *IEEE Transactions on Antennas and Propagation,* Vol. 14, No. 3, 1966, pp. 302-307, doi: 10.1109/TAP.1966.1138693

2.   Taflove, A., and Hagness, S. C., *Computational Electrodynamics: The Finite-Difference Time-Domain Method*, Artech House, 3rd ed., 2005.

3.   Jin, J., *The Finite Element Method in Electromagnetics*, John Wiley & Sons, 2nd ed., New York, 2002.

4.   Shang, J. S., and Fithen, R. M., "A Comparative Study of Characteristic-Based Algorithms for the Maxwell Equations," *Journal of Computational Physics,* Vol. 125, No. 2, 1996, pp. 378-394.

5.   Baumann, D., Fumeaux, C., and Vahldieck, R., "Field-Based Scattering-Matrix Extraction Scheme for the FVTD Method Exploiting a Flux-Splitting Algorithm," *IEEE Transactions on Microwave Theory and Techniques,* Vol. 53, No. 11, 2005, pp. 3595-3605, doi: 10.1109/tmtt.2005.857103.

6.   Fumeaux, C., Baumann, D., and Vahldieck, R., "Advanced FVTD Simulation of Dielectric Resonator Antennas and Feed Structures," *Applied Computational Electromagnetics Society Journal,* Vol. 19, No. 3, 2004, pp. 155-164.

7.   Munz, C. D., Schneider, R., and Voss, U., "A Finite-Volume Method for the Maxwell Equations in the Time Domain," *SIAM Journal on Scientific Computing,* Vol. 22, No. 2, 2000, pp. 449-475.

8.   Shankar, V., Hall, W. F., and Mohammadian, A. H., "A CFD-Based Finite-Volume Procedure for Computational Electromagnetics - Interdisciplinary Application of CFD Methods," *AIAA 89-1987-CP*, 1987.

9.   Shang, J. S., and Gaitonde, D., "Characteristic-Based, Time-Dependent Maxwell Equation Solvers on a General Curvilinear Frame," *AIAA Journal,* Vol. 33, No. 3, 1995, pp. 491-498.

10.   Barth, T. J., "Recent Developments in High Order K-Exact Reconstruction on Unstructured Meshes," *AIAA Paper 93-0668*, 1993.

11.   Ollivier-Gooch, C., Nejat, A., and Michalak, K., "Obtaining and Verifying High-Order Unstructured Finite Volume Solutions to the Euler Equations," *AIAA Journal,* Vol. 47, No. 9, 2009, pp. 2105-2120, doi: 10.2514/1.40585.

12.   Reed, W. H., and Hill, T. R., "Triangular Mesh Methods for the Neutron Transport Equation," *Los Alamos Scientific Laboratory Report LA-UR-73-479*, 1973.

13.   Bassi, F., Crivellini, A., Rebay, S., and Savini, M., "Discontinuous Galerkin Solution of the Reynolds-Averaged Navier-Stokes and K-Omega Turbulence Model Equations," *Computers & Fluids,* Vol. 34, No. 4-5, 2005, pp. 507-540, doi: 10.1016/j.compfluid.2003.08.004.

14.   Bassi, F., and Rebay, S., "High-Order Accurate Discontinuous Finite Element Solution of the 2D Euler Equations," *Journal of Computational Physics,* Vol. 138, No. 2, 1997, pp. 251-285.

15.   Diosady, L. T., and Darmofal, D. L., "Preconditioning Methods for Discontinuous Galerkin Solutions of the Navier-Stokes Equations," *Journal of Computational Physics,* Vol. 228, No. 11, 2009, pp. 3917-3935, doi: 10.1016/j.jcp.2009.02.035.

16.   Hesthaven, J. S., and Warburton, T., *Nodal Discontinuous Galerkin Methods, Algorithms, Analysis, and Applications*, Springer, 2008.

17.   Mavriplis, D. J., Wang, L., and Burgess, N., "Progress in High-Order Discontinuous Galerkin Methods for Aerospace Applications," *AIAA 2009-601, Presented at the 47th Aerospace Sciences Meeting, January 2-8*, 2009.

18.   Venkatakrishnan, V., Allmaras, S. R., Johnson, F. T., and Kamenetskii, D. S, "Higher Order Schemes for the Compressible Navier-Stokes Equations," *AIAA 2003-3987, Presented at the 16th AIAA Computational Fluid Dynamics Conference, Orlando, FL., June 23-26*, 2003.

19. Catella, A., Dolean, V., and Lanteri, S., "An Implicit Discontinuous Galerkin Time-Domain Method for Two-Dimensional Electromagnetic Wave Propagation," *COMPEL-the International Journal for Computation and Mathematics in Electrical and Electronic Engineering,* Vol. 29, No. 3, 2010, pp. 602-625, doi: 10.1108/03321641011028215.

20. Cockburn, B., Li, F. Y., and Shu, C. W., "Locally Divergence-Free Discontinuous Galerkin Methods for the Maxwell Equations," *Journal of Computational Physics,* Vol. 194, No. 2, 2004, pp. 588-610, doi: 10.1016/j.jcp.2003.09.007.

21. Gedney, S. D., Luo, C., Roden, J. A., Crawford, R. D., Guernsey, B., Miller, J. A., Kramer, T., and Lucas, E. W., "The Discontinuous Galerkin Finite-Element Time-Domain Method Solution of Maxwell's Equations," *Applied Computational Electromagnetics Society Journal,* Vol. 24, No. 2, 2009, pp. 129-142.

22. Hesthaven, J. S., and Warburton, T., "Nodal High-Order Methods on Unstructured Grids - I. Time-Domain Solution of Maxwell's Equations," *Journal of Computational Physics,* Vol. 181, No. 1, 2002, pp. 186-221, doi: 10.1006/jcph.2002.7118.

23. Ji, X., Lu, T., Cai, W., and Zhang, P. W., "Discontinuous Galerkin Time Domain (DGTD) Methods for the Study of 2-D Waveguide-Coupled Microring Resonators," *Journal of Lightwave Technology,* Vol. 23, No. 11, 2005, pp. 3864-3874, doi: 10.1109/jlt.2005.855858.

24. Kabakian, A. V., Shankar, V., and Hall, W. F., "Unstructured Grid-Based Discontinuous Galerkin Method for Broadband Electromagnetic Simulations," *Journal of Scientific Computing,* Vol. 20, No. 3, 2004, pp. 405-431.

25. Lu, T., Cai, W., and Zhang, P. W., "Discontinuous Galerkin Time-Domain Method for GPR Simulation in Dispersive Media," *IEEE Transactions on Geoscience and Remote Sensing,* Vol. 43, No. 1, 2005, pp. 72-80, doi: 10.1109/tgrs.2004.838350.

26. Lu, T., Zhang, P. W., and Cai, W., "Discontinuous Galerkin Methods for Dispersive and Lossy Maxwell's Equations and PML Boundary Conditions," *Journal of Computational Physics,* Vol. 200, No. 2, 2004, pp. 549-580, doi: 10.1016/j.jcp.2004.02.022.

27. Fahs, H., "Development of a HP-Like Discontinuous Galerkin Time-Domain Method on Non-Conforming Simplicial Meshes for Electromagnetic Wave Propagation," *International Journal of Numerical Analysis and Modeling,* Vol. 6, No. 2, 2009, pp. 193-216.

28. Hesthaven, J. S., and Warburton, T., "High-Order Accurate Methods for Time-Domain Electromagnetics," *Computer Modeling in Engineering & Sciences,* Vol. 5, No. 5, 2004, pp. 395-407.

29. Hesthaven, J. S., and Warburton, T., "High-Order Nodal Discontinuous Galerkin Methods for the Maxwell Eigenvalue Problem," *Philosophical Transactions of the Royal Society of London Series A-Mathematical Physical and Engineering Sciences,* Vol. 362, No. 1816, 2004, pp. 493-524, doi: 10.1098/rsta.2003.1332.

30. Brooks, A. N., and Hughes, T. J. R., "Streamline Upwind/Petrov-Galerkin Formulations for Convection Dominated Flows with Particular Emphasis on the Incompressible Navier-Stokes Equations," *Computational Methods in Applied Mechanics and Engineering,* Vol. 32, No. 1-3, 1982, pp. 199-259, doi: 10.1016/0045-7825(82)90071-8.

31. Franca, L. P., Frey, S. L., and Hughes, T. J. R.,, "Stabilized Finite Element Methods: I. Application to the Advective-Diffusive Model," *Computer Methods in Applied Mechanics and Engineering,* Vol. 95, No. 2, 1992, pp. 253-276, doi: 10.1016/0045-7825(92)90143-8.

32. Hughes, T. J. R., and Mallet, M., "A New Finite Element Formulation for Computational Fluid Dynamics III. The Generalized Streamline Operator for Multidimensional Advective-Diffusive Systems," *Computer Methods in Applied Mechanics and Engineering,* Vol. 58, No. 3, 1986, pp. 305-328.

33. Barth, T. J. "Numerical Methods for Gasdynamic Systems on Unstructured Meshes," *An Introduction to Recent Developments in Theory and Numerics for Conservation Laws*. Vol. 5, Springer, 1998, pp. 195-285.

34. Bonhaus, D. L., "A Higher Order Accurate Finite Element Method for Viscous Compressible Flows," *Ph.D. Thesis, Virginia Polytechnic Institute and State University*, 1998.

35. Hughes, T. J. R., Franca, L. P., and Hulbert, G. M., "A New Finite-Element Formulation for Computational Fluid-Dynamics VIII. The Galerkin Least-Squares Method for Advective-Diffusive Equations," *Computer Methods in Applied Mechanics and Engineering,* Vol. 73, No. 2, 1989, pp. 173-189.

36. Shakib, F., Hughes, T. J. R., and Johan, Z., "A New Finite-Element Formulation for Computational Fluid-Dynamics X. The Compressible Euler and Navier-Stokes Equations," *Computer Methods in Applied Mechanics and Engineering,* Vol. 89, No. 1-3, 1991, pp. 141-219.

37. Benbouza, N., Louai, F. Z., Drid, S., and Benoudjit, A., "Parameteric Analysis by the Meshless Local Petrov Galerkin (MLPG) Approach Applied to Electromagnetic Problems," *International Journal of Electrical and Power Engineering,* Vol. 1, No. 2, 2007, pp. 138-145.

38.	Viana, S. A., Rodger, D., and Lai, H. C., "Meshless Local Petrov-Galerkin Method with Radial Basis Functions Applied to Electromagnetics," *IEE-Proceedings-Science Measurement and Technology,* Vol. 151, No. 6, 2004, pp. 449-451, doi: 10.1049/ip-smt:20040860.
39.	Xu, E., X., Simkin, J., and Taylor, S., C., "Streamline Upwinding in a 3-D Edge-Element Method Modeling Eddy Currents in Moving Coordinates," *IEEE Transactions on Magnetics,* Vol. 42, No. 4, 2006, pp. 667-670, doi: 10.1109/TMAG.2006.871981.
40.	Soares, D., "Numerical Modelling of Electromagnetic Wave Propagation by Meshless Local Petrov-Galerkin Formulations," *CMES-Computer Modeling in Engineering & Sciences,* Vol. 50, No. 2, 2009, pp. 97-114.
41.	Harrington, R. F., *Time-Harmonic Electromagnetic Fields*, Wiley-IEEE Press, 2nd ed., 2001.
42.	Lorrain, P., Corson, D. R., and Lorrain, F., *Fundamentals of Electromagnetic Phenomena*, W. H. Freeman & Company, New York, 2000.
43.	Cockburn, B., Hou, S., and Shu, C.-W., "The Runge-Kutta Local Projection Discontinuous Galerkin Finite Element Method for Conservation Laws IV: The Multidimensional Case," *Mathematics of Computation,* Vol. 54, No. 190, 1990, pp. 545-581.
44.	Balanis, C. A., *Advanced Engineering Electromagnetics*, John Wiley & Sons, 1989.
45.	Iskander, M. F., *Electromagnetic Fields and Waves*, Waveland Press, Long Grove, 1992.
46.	Roe, P. L., "Approximate Riemann Solvers, Parameter Vectors, and Difference Schemes," *Journal of Computational Physics,* Vol. 43, No. 2, 1981, pp. 357-372, doi: 10.1016/0021-9991(81)90128-5.
47.	Saad, Y., and Schultz, "GMRES: A Generalized Minimal Residual Algorithm for Solving Nonsymmetric Linear Systems," *SIAM Journal of Scientific and Statistical Computing,* Vol. 7, No. 3, 1986, pp. 856-869.
48.	Saad, Y., *Iterative Methods for Sparse Linear Systems*, SIAM, 2nd ed., 2003.
49.	Rappaport, C. M., "Perfectly Matched Absorbing Boundary-Conditions Based on Anisotropic Lossy Mapping of Space," *IEEE Microwave and Guided Wave Letters,* Vol. 5, No. 3, 1995, pp. 90-92.
50.	Sacks, Z. S., Kingsland, D. M., Lee, R., and Lee, J. F., "A Perfectly Matched Anisotropic Absorber for Use as an Absorbing Boundary Condition," *IEEE Transactions on Antennas and Propagation,* Vol. 43, No. 12, 1995, pp. 1460-1463.
51.	Zhao, L., and Cangellaris, A. C., "A General Approach for the Development of Unsplit-Field Time-Domain Implementations of Perfectly Matched Layers for FDTD Grid Truncation," *IEEE Microwave and Guided Wave Letters,* Vol. 6, No. 5, 1996, pp. 209-211.
52.	Chew, W. C., Jin, J. M., and Michielssen, E., "Complex Coordinate Stretching as a Generalized Absorbing Boundary Condition," *Microwave and Optical Technology Letters,* Vol. 15, No. 6, 1997, pp. 363-369.
53.	Johnson, S. G., "Notes on Perfectly Matched Layers (PML)," *www-math.mit.edu/~stevenj/18.369/pml.pdf*, 2008.
54.	Cai, W., and Deng, S. Z., "An Upwinding Embedded Boundary Method for Maxwell's Equations in Media with Material Interfaces: 2D Case," *Journal of Computational Physics,* Vol. 190, No. 1, 2003, pp. 159-183, doi: 10.1016/s0021-9991(03)00269-9.
55.	www.guidedwavetech.com.
56.	Garcia-Castillo, L. E., Pardo, D., Gomez-Revuelto, I., and Demkowicz, L. F., "A Two-Dimensional Self-Adaptive HP Finite Element Method for the Characterization of Waveguide Discontinuities. Part I: Energy-Norm Based Automatic HP-Adaptivity," *Computer Methods in Applied Mechanics and Engineering,* Vol. 196, No. 49-52, 2007, pp. 4823-4852, doi: 10.1016/j.emzt.2007.06.024.
57.	Pardo, D., Garcia-Castillo, L. E., Demkowicz, L. F., and Torres-Verdin, C., "A Two-Dimensional Self-Adaptive HP Finite Element Method for the Characterization of Waveguide Discontinuities. Part II: Goal-Oriented HP-Adaptivity," *Computer Methods in Applied Mechanics and Engineering,* Vol. 196, No. 49-52, 2007, pp. 4811-4822, doi: 10.1016/j.cina.2007.06.023.
58.	Pozar, D. M., *Microwave Engineering*, John Wiley & Sons, 3rd ed., 2004.
59.	Ida, N., *Engineering Electromagnetics*, Springer-Verlag, 2nd ed., New York, 2004.
60.	Jiang, B. N., Wu, J., and Povinelli, L. A., "The Origin of Spurious Solutions in Computational Electromagnetics," *Journal of Computational Physics,* Vol. 125, No. 1, 1996, pp. 104-123.
61.	Lynch, D. R., and Paulsen, K. D., "Origin of Vector Parasites in Numerical Maxwell Solutions," *IEEE Transactions on Microwave Theory and Techniques,* Vol. 39, No. 3, 1991, pp. 383-394.
62.	Lynch, D. R., Paulsen, K. D., and Boyse, W. E., "Synthesis of Vector Parasites in Finite-Element Maxwell Solutions," *IEEE Transactions on Microwave Theory and Techniques,* Vol. 41, No. 8, 1993, pp. 1439-1448.
63.	Paulsen, K. D., and Lynch, D. R., "Elimination of Vector Parasites in Finite-Element Maxwell Solutions," *IEEE Transactions on Microwave Theory and Techniques,* Vol. 39, No. 3, 1991, pp. 395-404.

64.   Ise, K., Inoue, K., and Koshiba, M., "3-Dimensional Finite-Element Solution of Dielectric Scattering Obstacles in a Rectangular Wave-Guide," *IEEE Transactions on Microwave Theory and Techniques,* Vol. 38, No. 9, 1990, pp. 1352-1359.

65.   Assous, F., and Sonnendrucker, E., "Joly-Mercier Boundary Condition for the Finite Element Solution of 3D Maxwell Equations," *Mathematical and Computer Modelling,* Vol. 51, No. 7-8, 2010, pp. 935-943, doi: 10.1016/j.mcm.2009.08.027.

66.   www.ansoft.com/products/hf/hfss.

67.   Karypis, G., and Kumar, V., "A Fast and High Quality Multilevel Scheme for Partitioning Irregular Graphs," *SIAM Journal on Scientific Computing,* Vol. 20, No. 1, 1998, pp. 359-392.